Mitigation of coherent errors in the control of superconducting qubits with composite pulse sequences

Master's Thesis, 23.3.2023

Author:

OTTO SALMENKIVI

Supervisor:

JUHA MUHONEN
JAMI RÖNKKÖ (IQM FINLAND OY)

UNIVERSITY OF JYVÄSKYLÄ
DEPARTMENT OF PHYSICS

Abstract

Salmenkivi, Otto
Mitigation of coherent errors in the control of superconducting qubits with composite pulse sequences
Master's thesis
Department of Physics, University of Jyväskylä, 2023, 70 pages.

Superconducting circuits, which are used as a platform for quantum information processing, inherently suffer from noise and errors. In addition to decoherence, coherent errors in the quantum gate operations form a substantial error source in current quantum computing processors. These errors are typically only addressed with the calibration of control parameters. Fully compensating composite pulse sequences inspired by the NMR field have been identified as a possible measure to mitigate these errors in superconducting qubits. Here, the performance of two sequences, SCROFULOUS and BB1, applicable to an arbitrary single-qubit gate, is simulated and run on a 5-qubit IQM device. Both are able to correct for pulse amplitude errors on a wide range, but perform worse in terms of the accumulation of errors during multiple gates. It is concluded that the sequences do not offer benefits over standard calibration procedures since the native gate is the most accurate in the studied system.

Keywords: quantum information processing, superconducting qubit, error mitigation, composite pulse sequence

Tiivistelmä

Salmenkivi, Otto
Koherenttien virheiden vähentäminen suprajohtavien kubittien kontrollissa pulssisekvenssien avulla
Pro gradu -tutkielma
Fysiikan laitos, Jyväskylän yliopisto, 2023, 70 sivua

Kvanttilaskennan alustana käytettävät suprajohtavat kubitit kärsivät kohinasta ja virheistä. Dekoherenssin lisäksi kvanttiporttien koherentit virheet muodostavat merkittävän virhelähteen tämänhetkisissä kvanttitietokoneissa. Usein niiden vähentämisessä turvaudutaan systeemin kontolliparametrien tarkempaan kalibraatioon, mutta NMR-sovelluksista inspiroitujen pulssisekvenssien hyödyntämistä on myös ehdotettu. Tässä työssä tutkitaan kahden sekvenssimenetelmän, SCROFULOUS:n ja BB1:n, kykyä korjata kontrollipulssin systemaattista amplitudivirhettä hyödyntäen sekä simulaatioita että IQM:n viisikubittista kvanttitietokonetta. Molempien menetelmien todetaan korjaavan amplitudivirhettä laaja-alaisesti, mutta myös keräävän enemmän virhettä operaatioiden määrän kasvaessa. Pulssisekvenssit eivät mahdollista normaalia kalibraatiota tarkempia portteja, sillä natiiviportin todetaan olevan sekvenssejä tarkempi tutkitussa systeemissä.

Avainsanat: kvantti-informaatio, suprajohtava kubitti, pulssisekvenssi

Preface

This thesis marks the end of my five year studies towards a Master of Science degree in the University of Jyväskylä. As a graduate of the Nanoscience curriculum I now posses multidisciplinary knowledge not only about the fundamentals of the natural world, but also about the current status of technological developments. I have chosen to apply this knowledge in the field of quantum computing, and look forward to the many scientific experiences together.

I am grateful for IQM for commissioning this work. During my internship I have had the greatest opportunity to learn from experienced scientists, make new friends and connections, and to see first-hand the emergence of a new computational era that is quantum computing. It has been a great pleasure follow world-class people working towards the shared goal of quantum advantage. I thank Jami for the guidance with this thesis and everything else, Juha for supervising and offering valuable comments, and Caspar for his leadership.

I would also like to thank Veera, my family, and my friends for the continuous support and encouragement.

Jyväskylä March 23, 2023

Otto Salmenkivi

Contents

1 Introduction

Quantum computing represents a new computing paradigm with the promise of solving selected computational tasks that are unfeasible even for the most powerful classical computers [1]. This new way of computing was first conceptualised by Richard Feynmann in 1982 [2]; since the natural world follows the laws of quantum mechanics, it would also be most accurately simulated by a quantum-mechanical system. His words are often heralded as the birth of a scientific field: quantum information processing (QIP). In the decades since, quantum mechanical systems especially suited for QIP have been extensively studied at an accelerating pace. More recently, as the concept has matured theoretically and experimental demonstrations have been successfully carried out, the field has seen a surge of efforts and funding also in the private sector. A number of spin-offs have emerged from academia, and the largest information technology corporations are also allocating resources. Most, if not all, are competing to demonstrate quantum advantage, a feat of solving a computational problem significantly faster on a quantum computer compared to the classical counterpart. While the first may claim fortune and fame in the short term, the true motivation to pursue quantum computing is in the value the new technology will create during the decades to come. Scientifically and industrially attractive applications have been reported in the fields of cryptography [3], finance [4, 5], quantum chemistry [6, 7] and optimization related to multiple disciplines [8], among others. The field is living in the NISQ era (noisy intermediate-scale quantum), where devices are still subject to decoherence that limits their computational power, and the mitigation of noise and the development of noise-tolerant small-scale quantum algorithms are emphasized [9]. Large-scale adaptation of quantum computing would require quantum error-correction, where multiple physical qubits are combined to create logical units to achieve fault-tolerant quantum computation [1].

Multiple physical implementations to create a qubit, a two-level quantum system as the computing unit of a quantum computer, exist. One of the most widely adopted and promising candidate for large-scale quantum computation are superconducting electric circuits, and they are also the platform of choice for IQM, an European leader of the technology. Superconducting qubits have proven to achieve high fidelities and the manufacturing has benefited from the repurposing of known fabrication methods used in the semiconductor industry [10]. Out of the many different superconducting qubit types, the transmon (see Sec. 2.3.3) has shown great promise. Once manufactured, the qubits are cooled to millikelvin temperatures using dilution refrigerators to reveal quantum mechanical behaviour. The computation then requires precise control over the quantum states of the system, which is a complicated engineering task involving the understanding of circuit quantum electrodynamics (QED), electrical engineering, cryogenics and accompanying software.

This thesis discusses the error mitigation in superconducting quantum computers, more precisely, the use of composite pulse sequences to mitigate coherent errors in transmon qubits. Error mitigation deals with the development of qubits and controls that are less susceptible to the unavoidable quantum noise present in all systems, in contrast to quantum error correction using fault-tolerant logical qubits. Composite pulse sequences originate from nuclear magnetic resonance (NMR) field and aim to create excitation profiles that are robust against errors and dispersion in system parameters [11], and they have been shown to be compatible also with QIP error mitigation [12, 13]. The error mitigation efforts here are targeted at coherent errors in the microwave pulses creating single-qubit gates with the aim of cancelling systematic rotation errors. The two sequencing methods, SCROFULOUS [14] and BB1 [15], were chosen due to proven mitigation capability on a large error scale with only a small overhead in computation length, and their compatibility with the gate-level abstraction. Their effectiveness is investigated both with simulations and on a 5-qubit IQM quantum processor.

Classical simulations of quantum systems can reveal valuable insights into their inner workings. However, the simulated models are always trade-offs between the speed of calculation and the accuracy against the real physical world. In this work, the performance of the two composite pulses in comparison to the native gate is simulated in two ways: a less accurate and computationally lighter gate-level simulator is used to investigate their characteristics in a landscape of coherent and incoherent errors, while a more sophisticated pulse-level model is used to compare their performance in a more physically accurate way. Ideal gate-level simulation translates to simple matrix multiplication, though a simple noise model can be included by exponential decay functions based on the Bloch-Redfield model and their application through matrix exponentiation. In addition, qubits are always assumed to be true two-level systems. On the other hand, the pulse-level simulation includes a deeper level of physics. The quantum mechanical system is described by a Hamiltonian operator, which can be made to include time-dependent control terms, and the computation can be modelled by evolving the system in time. It also offers possibilities to include higher excitation states and more advanced noise models, e.g., pulse distortions and parasitic terms in the Hamiltonian. In a wider QIP context, the simulation of a quantum computer can be considered as a gateway into the new computational world for both the science community and private actors, and serve as an educational tool and a testbed for algorithms and error mitigation methods.

The pulse-level has recently seen a rising interest also from a resource optimisation perspective. The pulse-level physics have been a fundamental part of circuit QED since the very first devices; however, since the creation of systems with high qubit numbers, intrinsically long coherence times and and high gate fidelities have proven a difficult and expensive task, other approaches to extract the potential of current systems is being investigated. For example, known NISQ-relevant quantum algorithms can be made more hardware efficient by leaving the gate-level abstraction of matrix algebra and entering the lowest level of quantum control [16], and open-source tools for this approach have also been published [17].

Since this thesis addresses only single-qubit gates, the qubit-qubit interactions, such as two-qubit gates or unwanted crosstalk between qubits, will not be discussed. However, the capability to couple two qubits to perform quantum operations is a fundamental necessity in QIP, and two-qubit gates continue to be an active area of research and improvement. IQM has recently announced it's benchmark fidelity of above 99.8 % for a controlled-Z gate between two superconducting transmon qubits [18]. The approach utilises tunable coupling created by a third transmon circuit coupled to both computational qubits, and achieves high fidelities for larger qubit separation allowing more physical space for other components, such as readout resonators and microwave control lines.

The outline of the thesis is as follows. The theoretical background supporting the work is given in Sec. 2, where open quantum systems, the basics of quantum computing and superconducting qubits, especially the transmon and its control, are discussed. Also, details about noise in superconducting qubits, its quantitative measurement with fidelity and inclusion in simulation is presented. The section is concluded with the introduction of composite pulse sequences. Sec. 3 introduces the simulation tools and the quantum processing unit used, and Sec. 4 present the results of various performance revealing experiments. The work is concluded in Sec. 5.

2 Theoretical background

2.1 Open quantum systems

This section references Chapters 2 and 9 from the book by Nakahara and Ohmi [19].

A pure state in a quantum system can be completely described by $|\psi\rangle$, a normalised vector in Hilbert space $\mathcal{H}$, which is a complex space with a inner product $\langle\psi|\psi\rangle = 1$. Any superposition of such states, e.g. $c_1 |\psi_1\rangle + c_2 |\psi_2\rangle$, is also a valid pure state. In the Schrödinger picture of quantum mechanics the time evolution of a pure state is governed by the Schrödinger equation

$$i\hbar \frac{\partial |\psi\rangle}{\partial t} = \hat{H} |\psi\rangle \,, \tag{1}$$

where $\hbar$ is the reduced Planck constant, $\hat{H}$ a Hermitian operator called the Hamiltonian describing the systems energy. For a time-independent Hamiltonian it has a solution

$$|\psi(t)\rangle = e^{-i\hat{H}t/\hbar} |\psi(0)\rangle \,, \tag{2}$$

and, if Hamiltonian is time-dependent, the solution is

$$|\psi(t)\rangle = \mathcal{T} \exp -\frac{i}{\hbar} \int_0^t \hat{H}(t')dt' \, |\psi(0)\rangle \,, \tag{3}$$

where $\mathcal{T}$ is a time-ordering operator. The two equation above can both be written in terms of a unitary time-evolution operator as $|\psi(t)\rangle = \hat{U} |\psi(0)\rangle$. The unitarity condition $\hat{U}^\dagger \hat{U} = \hat{U}\hat{U}^\dagger = \mathbb{1}$ maintains the norm of the state.

A mixed state, on the other hand, describes a probabilistic ensemble, where a system is in a state $|\psi_i\rangle$ with probability p_i. This randomness means that the state is not known with certainly, but it is not to be mixed with the concept of quantum mechanical superposition. Also, a pure state is a special case for a mixed state with probability of one for only a single state. Mathematically a mixed state is described by the density matrix

$$\rho = \sum_{i=1}^{N} p_i \left|\psi_i\right\rangle \left\langle\psi_i\right|, \tag{4}$$

where N is the number of available states. The density matrix is positive semi-definite Hermitian operator with $\mathrm{Tr}(\rho) = 1$. Also, the state is pure if and only if $\rho^2 = \rho$. The density matrix evolves in time as defined by the Liouville-von Neumann equation as

$$i\hbar\frac{d}{dt}\rho = [\hat{H},\rho], \tag{5}$$

where the square brackets indicate the commutator. With $\hat{U}(t)$ being a general time-evolution operator, the density matrix can be propagated as

$$\rho(t) = \hat{U}(t)\rho(0)\hat{U}^{\dagger}(t). \tag{6}$$

For a time-independent Hamiltonian H the evolution can be solved from the Liouville-von Neumann equation as

$$\rho(t) = e^{-i\hat{H}t/\hbar}\rho(0)e^{i\hat{H}t/\hbar}, \tag{7}$$

resembling the evolution for a state vector.

An open quantum system is formed out of quantum mechanical system coupled to its environment. However, unlike in a closed system where the complete wave function of the system is known, the environment is often described as a bath, the states of which are at least partially unknown. The state of the entire system can be expressed as a tensor product

$$\rho = \rho_S \otimes \rho_E, \tag{8}$$

where ρ_S and ρ_E are the density matrices of the system and the environment, respectively. The density matrix of the system of interest can be separated by taking the partial trace $\rho_S = \mathrm{Tr}_E(\rho)$.

A quantum operator $\mathcal{L}$, that maps a density matrix to another linearly, is known as a superoperator. Moreover, $\mathcal{L}$ is completely positive and trace preserving (CPTP). Positivity requires that a positive operator is mapped to another positive operator in the same Hilbert space, and it is said to be complete, if the same is satisfied for an extension $\mathcal{L} \otimes \mathbb{1}_n$, for an arbitrary $n \in \mathbb{N}$. Trace preserving translates simply to $\mathrm{Tr}(\mathcal{L}\rho_S) = \mathrm{Tr}(\rho_S) = 1$.

Even though the Liouville-von Neumann equation in Eq. (5) holds for all systems, the Hamiltonian of the environment is often unknown or the combined system is too large for the equation to be used practically. Therefore a map like the one in Eq. (6) is not obvious. A common initial assumption is that the system has no memory, meaning that the evolution of $\rho(t)$ is governed solely by itself at time t, and passed events have a negligible effect in the future evolution. This assumption is known as the Markovian approximation. Using the superoperator formalism, the master equation describing the time evolution of a Markovian system is then

$$\frac{\partial}{\partial t}\rho_S = \mathcal{L}\rho_S. \tag{9}$$

Such evolution can be calculated using the Lindblad master equation

$$\frac{\partial}{\partial t}\rho_S = -\frac{i}{\hbar}\left[\hat{H},\rho_S\right] + \sum_{K=1}^{N}\gamma_K\left(\hat{L}_K\rho_S\hat{L}_K^\dagger - \frac{1}{2}\hat{L}_K^\dagger\hat{L}_K\rho_S - \frac{1}{2}\rho_S\hat{L}_K^\dagger\hat{L}_K\right), \tag{10}$$

where γ_K is related to the probability for a Lindblad operator $\hat{L}_K$ to manifest, or the rate at which $\hat{L}_K$ is applied. The Lindblad equation is used to solve non-unitary dynamics, characteristic for open quantum systems. An operator $\sqrt{\gamma_K}\hat{L}_K$ is often referred to as a collapse operator.

2.2 Basics of quantum computing

This section aims to provide the necessary information about quantum computation relevant in the scope of this work. Since this work discusses error mitigation on single qubit operations, the topics of multi-qubit gates, circuits and standard algorithms, although critical for the field, are mostly not discussed. The books by Nielsen and Chuang [1], Nakahara and Ohmi [19], and Mermin [20] cover the field of quantum computing extensively, are used as general reference in this section, and are referred to for more information.

The computational unit of quantum computing is the qubit, a quantum mechanical counterpart to the classical bit. Regardless of the physical implementation, the two orthonormal basis states of a qubit are $|0\rangle$ and $|1\rangle$. Any linear combination, or superposition, of these is also a valid qubit state, written as

$$|\psi\rangle = \alpha\,|0\rangle + \beta\,|1\rangle\,, \quad |\alpha|^2 + |\beta|^2 = 1, \tag{11}$$

where α and β are complex numbers satisfying the normalization condition relating to the measurement probabilities $|\alpha|^2$ and $|\beta|^2$ of the two states. Due to the normalization, the qubit state can be equivalently given as

$$|\psi(\theta, \varphi)\rangle = e^{i\varphi_\alpha} \cos\frac{\theta}{2} |0\rangle + e^{i\varphi_\beta} \sin\frac{\theta}{2} |1\rangle = \cos\frac{\theta}{2} |0\rangle + e^{i\varphi} \sin\frac{\theta}{2} |1\rangle \, , \tag{12}$$

where the second equality omits the unobservable global phase and fixes the coefficient of $|0\rangle$ real. Moreover, this gives rise to a widely used graphical representation known as the Bloch sphere, illustrated in Fig. 1. The unit vector representing the state on the sphere is called the Bloch vector, defined as

$$\hat{n}(\theta,\varphi) = (\sin\theta\cos\varphi, \sin\theta\sin\varphi, \cos\theta)^\top . \tag{13}$$

By defining a vector $\vec{\sigma} = (\sigma_x, \sigma_y, \sigma_z)$ with Pauli matrices

$$\sigma_x = \begin{bmatrix} 0 & 1 \\ 1 & 0 \end{bmatrix} \qquad \sigma_y = \begin{bmatrix} 0 & -i \\ i & 0 \end{bmatrix} \qquad \sigma_z = \begin{bmatrix} 1 & 0 \\ 0 & -1 \end{bmatrix} , \tag{14}$$

one can show that $|\psi(\theta,\varphi)\rangle$ is an eigenstate of $\hat{n}(\theta,\varphi) \cdot \vec{\sigma}$ with an eigenvalue $+1$. When $0 \leq \theta \leq \pi$ and $0 \leq \varphi < 2\pi$, the state corresponds to a unique point on the sphere.

A similar representation exist also for mixed states, described by the density matrix ρ. A general form for ρ can be written as a linear combination

$$\rho = \frac{1}{2} \left(\mathbb{1} + u_x\sigma_x + u_y\sigma_y + u_z\sigma_z \right) , \tag{15}$$

where the coefficients u_i form a real vector $\vec{u}$, for which $|\vec{u}| \leq 1$. If $|\vec{u}| = 1$, the vector lies on the unit sphere as thus corresponds to a pure state. On the contrary, when $|\vec{u}| < 1$, the point lies within the unit ball, called the Bloch ball, and represents a mixed state. Therefore $\hat{n}$ is a special case of $\vec{u}$ limited to pure states. From a visualisation point of view, the decoherence of a quantum state can be seen as the decrease in the lenght of $\vec{u}$, i.e. the vector shrinks to the center of the Bloch ball.

The qubit can also be thought as a vector in $\mathbb{C}^2$, in which the basis states

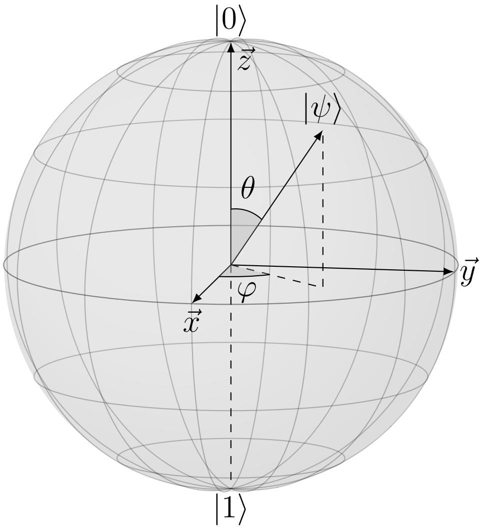

Figure 1. The Bloch sphere representing the quantum state $|\psi\rangle$ of a two-level system, described by the Bloch vector $\hat{n}(\theta, \varphi)$, where θ and φ are the polar and azimuthal angles, respectively.

corresponding to basis vectors as

$$|0\rangle \Leftrightarrow \begin{bmatrix} 1 \\ 0 \end{bmatrix} \qquad |1\rangle \Leftrightarrow \begin{bmatrix} 0 \\ 1 \end{bmatrix}. \tag{16}$$

Quantum operators acting on this two-level system are described 2×2 matrices, that are also known as gates within the abstraction of gate based quantum computing. Such operators U preserve the norm of the vector, resulting in the unitarity conditions $UU^\dagger = U^\dagger U = \mathbb{1}$. Universal quantum computing requires, at least in theory, exact control of the state vector over the Bloch sphere. This can be achieved with rotation operators defined with Pauli matrices as $R_i(\theta) = \exp(-i\theta\sigma_i/2)$, with $i \in \{x,y,x\}$. The Pauli gates are often denoted by X, Y and Z, with a subscript to indicate a parametrized rotation, e.g. $\mathsf{X}_{\frac{\pi}{2}}$ for a $\pi/2$ rotation around the x-axis.

A gate set is said to be universal for quantum computation, if any unitary operation can be executed to an arbitrary accuracy with a circuit involving only those gates. For a multi-qubit system a universal gate set is formed out of the CNOT gate, i.e. a controlled X gate, and arbitrary control over the single qubit state. The latter can be achieved by the three Pauli rotation matrices. One solution is to combine the x and y rotations to a rotation around an arbitrary axis along the

xy-plane of the Bloch sphere. This is referred here as a PRX gate defined as

$$\mathrm{PRX}(\theta,\varphi) = \exp\left(-i\frac{\theta}{2}(\sigma_x\cos\varphi + \sigma_y\sin\varphi)\right) = \begin{bmatrix} \cos\frac{\theta}{2} & -ie^{-i\varphi}\sin\frac{\theta}{2} \\ -ie^{i\varphi}\sin\frac{\theta}{2} & \cos\frac{\theta}{2} \end{bmatrix}. \tag{17}$$

The rotation angles can be related to the Bloch sphere by noting that

$$\mathrm{PRX}\left(\theta, \varphi + \frac{\pi}{2}\right)|0\rangle = \cos\frac{\theta}{2}|0\rangle + e^{i\varphi}\sin\frac{\theta}{2}|1\rangle. \tag{18}$$

With the added knowledge that $\sigma_x\sigma_y = i\sigma_z$, the z rotations could be decomposed as x and y. However, other more efficient methods exist.

Rotations around the z-axis can be implemented in multiple ways. In the physical devices one can tune the frequency of the qubit away from the operating point for some time period, which effectively rotates the qubit. The tuning can be achieved, for example, by introducing a strongly detuned microwave control pulse, which induces an ac-Stark shift in the frequency, or simply by changing the magnetic field in flux-tunable qubits [21, 22]. However, a simpler mathematical method is provided by virtual Z gates, where the original rotation angle around the z-axis is subsumed into the x and y rotations of the following gates. It can also be thought as rotating the axes during the circuit and re-evaluating the parameters of the following gates. Following the example by McKay *et al.* [23], the effect of a virtual Z gate can be highlighted by starting with a sequence of two gates: X_θ as a parameterized rotation around the x-axis followed by a $\mathsf{X}_\theta^\varphi$ rotation, where the superscript notes that the rotation axis is offset by φ. Using time ordering from right to left, the sequence is then

$$\begin{aligned} \mathsf{X}_\theta^\varphi\mathsf{X}_\theta &= \exp\left(-i\frac{\theta}{2}(\sigma_x\cos\varphi + \sigma_y\sin\varphi)\right)\mathsf{X}_\theta && (19) \\ &= \exp\left(i\frac{\varphi}{2}\sigma_z\right)\exp\left(-i\frac{\theta}{2}\sigma_x\right)\exp\left(-i\frac{\varphi}{2}\sigma_z\right)\mathsf{X}_\theta && (20) \\ &= \mathsf{Z}_{-\varphi}\mathsf{X}_\theta\mathsf{Z}_\varphi\mathsf{X}_\theta, && (21) \end{aligned}$$

where the Euler's formula and few other trigonometric identities were used. Assuming no gates are performed afterwards, the final rotation has no measurable effect since the qubit is measured along the z-axis. Thus, it is shown that a Z_φ rotation is effectively equal to changing the rotation axis of the following gate by φ. Furthermore, any single qubit circuit containing arbitrary gates U_i and Z gates can be analytically modified to remove all Z gates. A circuit of form

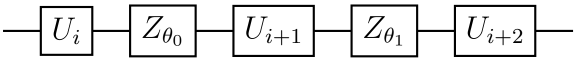

is equivalently transformed to

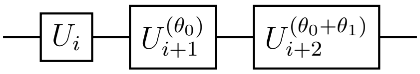

.

As seen above, quantum gates are often visualised using the circuit model, first introduced by Deutsch [24]. Qubits are represented as horizontal wires, and operations as boxes operated from left to right, contrary to the mathematical ordering of operations. The model is convenient for representing larger circuits and small algorithms, where multiqubit gates can be represented vertically, and measurement and classical bits can be included.

2.3 Superconducting qubits

2.3.1 Superconductivity and Josephson junctions

The circuit based quantum computing relies heavily on the quantum mechanical phenomenon of superconductivity. It was first discovered by Heike Kamerlingh Onnes in 1911, when indentifying the zero-resistance of mercury at temperatures of few Kelvins [25], and theoretically formulated to the BCS theory more than forty years later by Baarden, Cooper and Schrieffer [26] in 1957. The most noticeable effects of superconductivity are the capability to carry electrical current without dissipation and the Meissner effect. In the latter, magnetic flux created by a constant external magnetic field is expelled from the material as it transitions to the superconducting state. This is facilitated by persistent supercurrent loops on superconductor's surface, which in turn create an opposing magnetic field leading to repulsion. This leads to a superconductors being perfect diamagnets. The characteristic length during which the magnetic field exponentially decays in the superconductor is called the London penetration depth. Both of these effects have upper limits after which they disappear; the superconducting state breaks if current exceeds the critical current I_c or if the magnetic field exceeds the critical field H_c. In general, superconductivity is a phase transformation that happens for many metals below a critical temperature T_c. [27]

The BCS theory is based on the assumption that in the superconducting state electrons exhibit attractive interactions due to electron-phonon coupling and become correlated. These correlated electron pairs are referred to as Cooper pairs. Phenomenologically the phonon-mediated attraction can be though of in terms of Coulombic interactions as follows: 1) A moving electron disturbs the fixed lattice ions as it passes by, but the distortion in the ion positions lags behind due to their larger mass. 2) Meanwhile the electron moves away from the lattice site. 3) A second electron enters the proximity of the disturbed ions and experiences an attractive force towards the perturbed ion without a major repulsion from the first electron. These steps can result in an effective electron-electron attraction between distant electrons.

When two metals in superconducting state are weakly connected, typically with a thin non-conducting layer, Cooper pairs may tunnel quantum mechanically through the barrier resulting in the Josephson effect. The phenomenon can be captured in two equations. The dc Josephson relation reads

$$I = I_c \sin\phi, \tag{22}$$

where I_c is the structure-dependent critical current and ϕ the phase difference of the superconducting order parameter over the junction. Physically it describes that, even in the absence of a voltage drop, a current of a maximum amplitude I_c can form over the junction. Furthermore, the ac Josephson relation is defined as

$$\dot{\phi} = \frac{2eV}{\hbar}, \tag{23}$$

with $2e$ capturing the charge of a Cooper pair and V being the voltage over the junction. Solving the previous for ϕ and substituting to the dc relation gives

$$I = I_c \sin\left(\frac{2eV}{\hbar}t + \phi(0)\right), \tag{24}$$

showing that a constant voltage over the junction generates an oscillating current.

The Josephson dynamics are leveraged in mesoscopic stuctures called Josephson junctions, typically created between two metallic nanoscale leads separated by a metal oxide, e.g. Al$-$AlO$_x-$Al. The prevalence of the quantum mechanical Josephson effects make them useful in many fields, such as quantum sensing and quantum

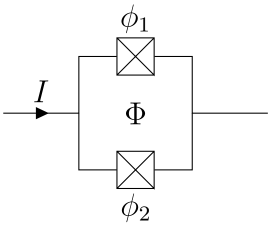

Figure 2. The lumped element circuit diagram of a dc-SQUID, where ϕ_i indicate the phase differences over the junctions and Φ the magnetic flux through the superconducting loop.

information processing.

The potential energy stored in a Josephson junction can be derived by integrating the instantaneous power $P = IV$ over the junction over time. Using the Josephson relations in Eqs. (22) and (23) it is

$$U(\phi) = \int IV dt = \int I_c \sin(\phi) \frac{\hbar}{2e} \dot{\phi} dt = -\underbrace{\frac{\hbar I_c}{2e}}_{=E_J} \cos(\phi) + \text{const.}, \tag{25}$$

where the Josephson energy E_J is identified, and the constant term represents an arbitrary energy shift, that can be neglected.

Superconducting quantum interference devices, or SQUIDs, have proven useful in many applications. A dc-SQUID, most relevant here, is formed from a conducting loop containing two Josephson junctions, with each junction forming a possible path for an external current to pass through, schematically presented in Fig. 2. SQUIDs are highly sensitivity in the magnetic flux through the loop and the current within it, one always being affected by the other.

The dependency of the current on the magnetic flux can be investigated via the superconducting order parameter. The gauge-invariant phase between points A and B on opposite sides of the junction is

$$\phi = \phi_{AB} - \frac{2\pi}{\Phi_0} \int_A^B \vec{A} \cdot \vec{dl}, \tag{26}$$

where ϕ_{AB} is the junction specific phase difference, $\Phi_0 = h/(2e)$ is the flux quantum of the Cooper pair and the vector potential $\vec{A}$ is integrated over the superconductor

[27]. In the structure of Fig. 2, the total phase in a cycle over the loop is

$$\begin{aligned} \phi_{\text{tot}} &= \phi_1 - \frac{2\pi}{\Phi_0}\int_1^2 \vec{A}\cdot\vec{dl} - \phi_2 - \frac{2\pi}{\Phi_0}\int_1^2 \vec{A}\cdot\vec{dl} \\ &= \phi_1 - \phi_2 - \frac{2\pi}{\Phi_0}\oint \vec{A}\cdot\vec{dl} = \phi_1 - \phi_2 - \frac{2\pi\Phi}{\Phi_0}. \end{aligned} \tag{27}$$

The total phase acquired over a single loop needs to be a multiple of 2π and therefore

$$\phi_1 - \phi_2 = \frac{2\pi\Phi}{\Phi_0} \mod 2\pi. \tag{28}$$

In the dc-SQUID the current can flow through either of the paths, each with an Josephson junction with critical current $I_{C,i}$ and phase difference ϕ_i, thus the total current is

$$I = I_{C,1}\sin(\phi_1) + I_{C,2}\sin\left(\phi_1 - \frac{\pi\Phi}{\Phi_0}\right). \tag{29}$$

The current that can flow through a dc-SQUID is seen to be a function of the magnetic flux. Assuming identical junctions with $I_{C,1} = I_{C,2} \equiv I_c$, the current simplifies to

$$I = 2I_c \sin\left(\phi_1 - \frac{\pi\Phi}{\Phi_0}\right)\cos\left(\frac{\pi\Phi}{\Phi_0}\right). \tag{30}$$

The critical current of a Josephson junction, or a dc-SQUID for that matter, describes the maximum current that can flow without a potential drop over the structure. The maximum current of the dc-SQUID can be investigated by setting the derivative with respect to ϕ_1 to zero,

$$\frac{dI_c}{d\phi_1} = 0 \quad\Leftrightarrow\quad 2I_c\cos\left(\phi_1 - \frac{\pi\Phi}{\Phi_0}\right)\cos\left(\frac{\pi\Phi}{\Phi_0}\right) = 0, \tag{31}$$

from which one can identify that $\cos(\phi_1 - \pi\Phi/\Phi_0) = 0$ is required. This translates to $\sin(\phi_1 - \pi\Phi/\Phi_0) = \pm 1$. The maximum current determined from Eq. (30) is therefore

$$I = 2I_c\left|\cos\left(\frac{\pi\Phi}{\Phi_0}\right)\right|. \tag{32}$$

2.3.2 LC circuit as a quantum harmonic oscillator

The physical characterization of a superconducting qubit usually starts as a simple classical LC resonator circuit. The derivation and the relevant system coordinates are then quantized to yield a quantum harmonic oscillator (QHO). However, a standard QHO has evenly spaced energy states, a fact that poses considerable issues for quantum computation, where an isolated two-level quantum system is needed. The two lowest states can however be separated from the rest by introducing non-linearity into the system. [28]

The classical Hamiltonian describing the energy of an LC circuit is

$$H = \frac{Q^2}{2C} + \frac{\Phi^2}{2L}, \tag{33}$$

where Q is the charge on the capacitor and Φ is the flux through the inductor. The same circuit can be treated quantum mechanically by promoting Q and Φ to quantum operators $\hat{Q}$ and $\hat{\Phi}$, which satisfy a commutation relation

$$[\hat{\Phi}, \hat{Q}] = \hat{\Phi}\hat{Q} - \hat{Q}\hat{\Phi} = i\hbar. \tag{34}$$

The operators also satisfy

$$\hat{\Phi} = \Phi_{\text{zpf}}(\hat{a}^\dagger + \hat{a}), \quad \hat{Q} = iQ_{\text{zpf}}(\hat{a}^\dagger - \hat{a}), \tag{35}$$

where $\hat{a}^\dagger$ and $\hat{a}$ are the creation and annihilation operators, respectively, and the zero-point fluctuations are $\Phi_{\text{zpf}} = \sqrt{\hbar Z/2}$ and $Q_{\text{zpf}} = \sqrt{\hbar/(2Z)}$, in which $Z = \sqrt{L/C}$ is the characteristic impedance of the oscillator [21].

Omitting the hats on the operators and using the reduced quantities $n = Q/(2e)$ and $\phi = 2\pi\Phi/\Phi_0$ for charge and flux operators respectively, the quantum mechanical Hamiltonian can then be defined as

$$H = 4E_C n^2 + \frac{1}{2}E_L\phi^2, \tag{36}$$

where a charging energy $E_C = e^2/2C$ and an inductive energy $E_L = (\Phi_0/2\pi)^2/L$ are introduced. The system has an infinite number of eigenstates $|k\rangle, k \in \{0,1,2,\ldots\}$ with evenly spaced eigenvalues E_k. The spacing is $E_{k+1} - E_k = \hbar\omega_r$, where $\omega_r = \sqrt{8E_LE_C}/\hbar = 1/\sqrt{LC}$ is the resonant frequency of the circuit. The discussion can be simplified by using the second quantization of the QHO, transforming the Hamiltonian into [28]

$$H = \hbar\omega_r \left(a^\dagger a + \frac{1}{2} \right). \tag{37}$$

For the eigenstates $|k\rangle$ of the QHO these ladder operators give $a^\dagger |k\rangle = \sqrt{k+1}\,|k+1\rangle$ and $a\,|k\rangle = \sqrt{k}\,|k-1\rangle$.

2.3.3 The superconducting transmon qubit

The non-linearity can be introduced to the LC circuit by replacing the inductor with a Josephson junction, a key element in the creation of superconducting circuits (see Sec. 2.3.1). The inductive energy term in the system Hamiltonian changes to the one for a Josephson junction from Eq. (25), and thus the Hamiltonian of this non-linear oscillator is

$$H = 4E_C n^2 - E_J \cos\phi. \tag{38}$$

The capacitive energy now includes the self-capacitance of the Josephson structure C_J, caused by finite leads connecting the junction. In this structure the Josephson junction is said to be shunted by the parallel capacitor, the capacitance of which is called the shunt capacitance C_s. Therefore the total charging energy $E_C = e^2/2C_\Sigma$, where $C_\Sigma = C_s + C_J$. The Josephson energy is defined as $E_J = I_c\Phi_0/2\pi = I_c\hbar/(2e)$. The physical non-linear spacing of the energy spectrum is mathematically captured by the cosinusoidal term, and is key in creating the non-degenerate transition energies. [28]

Using the second quantization, the Hamiltonian of Eq. (38) can be approximated as a Duffing oscillator in the ladder operator notation as

$$H = \omega_q a^\dagger a + \frac{\alpha}{2} a^\dagger a^\dagger a a, \tag{39}$$

where ω_q is now the qubit frequency and α is the anharmonicity defined as the difference in excitation between ground to first and from first to second excited state, i.e. $\alpha = \omega_q^{1\to2} - \omega_q^{0\to1}$[28]. The Hamiltonian also omits the reduced Planck's constants, since it is equivalent to discuss the dynamics in terms of eigenfrequencies. For a two-level system, the second term in Eq. (39) vanishes and a constant term can be omitted to give $H = -\omega_q\sigma_z/2$. For a three dimensional system it offsets the second excitation by α.

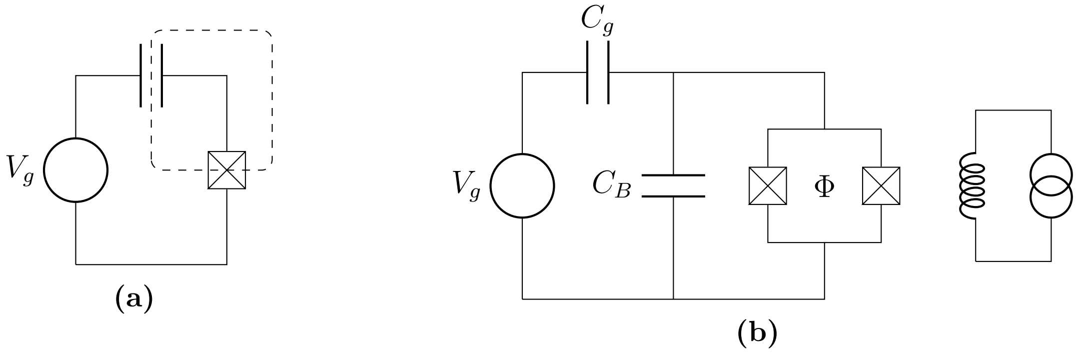

Figure 3. (a) The circuit diagram of a Cooper pair box, where the dashed box represents the superconducting island. (b) A reduced circuit of a tunable transmon qubit with an effective gate capacitance C_g, a shunt capacitance C_B and a dc-SQUID, the characteristics of which can be tuned with the magnetic environment, represented with the coil. The circuit omits the superconducting transmission line resonator for readout, which could be modeled as a LC oscillator parallel to C_B. [30]

A hallmark of superconducting qubits is that even as macroscopic systems they exhibit quantum mechanical behaviour, that can be engineered and exploited. In a Cooper pair box, illustrated in Fig 3a, from which all of the different qubit circuits have been derived, this happens in multiple ways. Firstly, in the superconducting state all electrons in the island form Cooper pairs and condense into a lower energy macroscopic ground state, which is separated from higher energy states by the superconducting gap Δ. As long as the charging energy E_C is lower than the superconducting gap Δ, the lowest available energy excitation in the system is the tunneling of a Cooper pair through the Josephson junction to the island. In addition, by increasing the capacitively controlled charging energy E_C over the Josephson energy E_J and the average thermal energy k_bT, fluctuations in the number of Cooper pairs in the island can be suppressed. An effective two level system can be created by taking account only the two lowest charge states. The energies of these states can further be tuned by introducing a voltage V_g to the gate electrode.[29] The gate charge $Q_g = C_gV_g$, where C_g and V_g are the gate capacitance and voltage, respectively, in addition to an environment-induced charge Q_r, transform the number operator of Cooper pairs in the Hamiltonian of Eq. (38) into $n - n_g$, where $n_g = (Q_g + Q_r)/(2e)$ [30].

The system characteristics of a superconducting qubit is in large part dependent on the balance between the two terms in Eq. (38), meaning the ratio between the Josephson and the charging energies. [28]. The first functional realization of superconducting qubits, the charge qubit in 1999 [29], was designed to work in the $E_J \leq E_C$ regime, where in general the system is more susceptible to fluctations in the charge, i.e. charge noise. The E_J/E_C ratio also dictates the charge dispersion and the anharmonicity. Charge dispersion captures the variation in the energy levels as a function of charge on the island, that can be due to unintended environmental effects or an applied gate voltage. A small dispersion, where the qubit frequency is less sensitive to changes in charge and fluctuations in it, is often aimed for. Higher E_J/E_C does decrease charge dispersion, but it simultaneously lowers the anharmonicity. However, the charge dispersion is reduced exponentially as the ratio is increased, while the anharmonicity decreases only by weak power law. [30]

One of the qubit schemes within the family of superconducting qubits that has shown the most promise and gained the most attraction is the transmon, presented by Koch *et al.* [30] in 2007. It shunts the junction by a large capacitance which decreases the charging energy of the island. This places transmon to the large E_J/E_C regime, values ranging from tens to a few hundreds. This has great operational benefits, as mentionded above. In the transmon architecture the charge dispersion is suppressed leading to more frequency stable qubits at a small cost in the qubit anharmonicity. Instead of using the number of Cooper pairs on the island as the discrete quantum number, transmon type qubits use the superconducting phase, which in the relevant energy limit has small quantum fluctuations and resembles a QHO solution to a local potential well. This is seen by expanding the cosine term in the Hamiltonian of Eq. (38) up to the fourth order as

$$E_J \cos\phi = \frac{1}{2}E_J\phi^2 - \frac{1}{24}E_J\phi^4 + \mathcal{O}(\phi^6). \tag{40}$$

Cutting to the first term would reveal a linear system, but the non-linearity is captured by the higher order terms. A noticeable remark is the negative coefficient for the second term, which leads to $\omega_q^{1\to 2} < \omega_q^{0\to 1}$, i.e. negative anharmonicity, and in general to decreasing transition frequencies for higher excitations. For transmons anharmonicity $\alpha \approx -E_C$ and is typically around 100-300 MHz and the qubit frequencies, given by $\omega_q = (\sqrt{8E_JE_C} - E_C)/\hbar$, are around 3 - 6 GHz. The lumped element transmon circuit diagram is presented in Fig. 3b.

The qubits can be made frequency tunable, which is useful for adjusting the coupling between neighbouring qubits by bringing them into and out of resonance. This is facilitated by replacing the single Josephson junction of early Cooper pair boxes by a dc-SQUID, presented in Sec. 2.3.1. This was included already in the first transmon qubit, but can also be referred to as an split transmon [30]. Assuming symmetric Josephson junctions each with a Josephson energy E_J, though not a trivial task for modern fabrication methods [31], the circuit Hamiltonian is transformed to

$$H = 4E_C n^2 - 2E_J |\cos\varphi_e| \cos\phi, \tag{41}$$

where the $\varphi_e = \pi\Phi_{\mathrm{ext}}/\Phi_0$. Thus the total Josephson energy $2E_J|\cos\varphi_e|$ is periodic in the external magnetic field, while getting values between zero and $2E_J$. [30] The dc-SQUID therefore creates a frequency controllable qubit. Again, the system can be approximated as a Duffing oscillator (Eq. (39), now with the added knowledge that the qubit frequency is tunable.

2.3.4 Single-qubit gates with capacitive control

In order to compute with qubits, their states need to be controllable through quantum operations. Single-qubit gates are applied to transmons by capacitively coupled superconducting microwave drivelines routed to the proximity of the transmon circuit. Starting from a LC oscillator point of view, the drive can be incorporated to the circuit Hamiltonian. For that, the driving voltage $V_d(t)$, the total capacitance to the ground $C_\Sigma = C + C_d$, where C_d is drive capacitance, and the time-dependent, renormalized charge variable $\tilde{Q}(t) = C_\Sigma\dot{\Phi} - C_d V_d(t)$ are introduced. The Hamiltonian is then defined as

$$H = \frac{\tilde{Q}(t)^2}{2C_\Sigma} + \frac{\Phi^2}{2L} + \frac{C_d}{C_\Sigma} V_d(t)\tilde{Q} \approx H_{\mathrm{LC}} + \frac{C_d}{C_\Sigma} V_d(t) Q, \tag{42}$$

where the approximation is valid in the weak coupling limit, i.e. when $\tilde{Q} \approx Q$ and H_{LC} is the LC oscillator Hamiltonian from Eq. (36). The charge variable is quantized, $Q = -iQ_{\mathrm{zpf}}(a - a^\dagger)$, as per Eq. (35). [28]

The control dynamics of a nonlinear superconducting qubit can be presented by replacing the H_{LC} with the one of a Josephson junction. Within the second quantization then, H_{LC} is replaced by the Hamiltonian of a Duffing oscillator of Eq.

(39), giving

$$H = \omega_q a^\dagger a + \frac{\alpha}{2} a^\dagger a^\dagger a a - i\Omega V_d(t)(a - a^\dagger), \tag{43}$$

where $\Omega = (C_d/C_\Sigma)Q_{\text{zpf}}$. For a two-level system, the previous simplifies to

$$H = -\frac{\omega_q}{2}\sigma_z + \Omega V_d(t)\sigma_y. \tag{44}$$

From the two-level Hamiltonian one can derive that, at zero control voltage, the qubit rotates around the z-axis of the Bloch sphere at a constant frequency ω_q. In order to simplify the description, the rotating frame is introduced to cancel the leading terms in Eqs. (43) and (44). In the two-level Bloch sphere picture, the rotation of the Bloch vector around the sphere is transformed into a frame rotating together with the vector, effectively creating a stationary state. In Appendix A it is shown that the rotating frame Hamiltonian is

$$H_{\text{rf}} = \frac{\alpha}{2} a^\dagger a^\dagger a a + \Omega V_d(t) \left[\cos\omega t(-i(a - a^\dagger)) - \sin\omega t(a + a^\dagger)\right], \tag{45}$$

which again simplifies in the two lowest levels to

$$H_{\text{rf}} = \Omega V_d(t) \left[\sigma_y \cos\omega t - \sigma_x \sin\omega t\right]. \tag{46}$$

The external driving voltage typically has a form

$$\begin{align} V_d(t) &= V_0 v(t) = V_0 s(t) \sin\left(\omega_d t + \phi\right) \tag{47}\\ &= V_0 s(t)(\underbrace{\cos\left(\phi\right)}_{=I} \sin\left(\omega_d t\right) + \underbrace{\sin\left(\phi\right)}_{=Q} \cos\left(\omega_d t\right)), \tag{48}\end{align}$$

where V_0 is the amplitude of the signal, and the in-phase and out-of-phase components I and Q are identified. By substituting this into the rotating frame Hamiltonian in Eq. (45), it becomes

$$H_{\text{rf}} = \frac{\alpha}{2} a^\dagger a^\dagger a a - \frac{\Omega V_0 s(t)}{2} \left[I(a + a^\dagger) + Q(-i(a - a^\dagger))\right], \tag{49}$$

where on-resonant driving is assumed. The change of frame also creates terms oscillating at twice the qubit or drive frequency, and these fast-rotating terms have been neglected. This is referred to as the rotating wave approximation. The second term still describes the control and is investigated next. For simplicity the constants

Ω and V_0 are subsumed into the envelope function $s(t)$.

The time-dependent effect of the driving Hamiltonian H_d can be expressed as the unitary operator

$$U(t) = \exp\left(-i\int_0^t H_d(t')dt'\right). \tag{50}$$

By substituting the Hamiltonian term the propagator reads

$$U(t) = \exp\left(\frac{i}{2}\left(I(a+a^\dagger) + Q(-i(a-a^\dagger))\right)\int_0^t s(t')dt'\right). \tag{51}$$

Assuming an in-phase signal with $\phi = 0$ and remembering that a general rotation operator can be expressed with exponentiated Pauli matrices, the integral above can be interpreted as rotation around x-axis by the angle

$$\theta(t) = -\int_0^t s(t')dt'. \tag{52}$$

With an out-of-phase signal with $\phi = \pi/2$, the same rotation would be achieved with respect to the y-axis. Therefore, by tuning the signal's phase and the envelope function, one can achieve arbitrary control over the two axes, making all single qubit operations possible.

The form of the envelope function has not yet been specified. In order to minimize the critical execution time and thus the effects of decoherence, a square pulse with constant amplitude would be the most effective. However, such an abrupt pulse shape is more prone to deformation in the control electronics, and moreover, the high frequency components can drive unwanted excitations. [21] Thus smoother pulse shapes are commonly used, such as a Gaussian waveform, but they do pose another issue. Depending on the width of the pulse, i.e. the standard deviation in the Gaussian case, the spectral composition can have a substantial amplitude spread around the intended drive frequency. In weakly anharmonic qubits, the amplitude can also be significant at the anharmonicity point, driving the second excitation. This leads to both leakage and phase errors. [28] A popular method to mitigate such errors is the DRAG (derivative reduction by adiabatic gate) scheme [32, 33]. The key is to modify the envelope function acting on the out-of-phase component Q: $s(t)$ is replaced by $\lambda\dot{s}(t)/\alpha$, where λ is a dimensionless scaling parameter and α is the qubit anharmonicity. In order to minimize leakage errors λ is set to 1, but the compromise between phase errors (minimized at $\lambda = 0.5$) and leakage can by tuned specifically for the device in question.

2.3.5 Initialization and measurement

The qubit control discussed in the previous section demonstrated the importance of qubit addressability. In addition to state manipulation, the qubit systems need to be addressed in two other ways, mentioned also in DiVincenzo's five criteria [34]: qubits need to reliably initialised and measured with high fidelity. Most often quantum algorithms starts with the assumption of qubits being in the state $|0\rangle$ that is mapped to the qubit's ground state. This is convenient, because in the absence of excitations, the physical apparatus can be thermally driven to the ground state.

The conventional method for initializing the qubits to the ground state relies on thermalization due to uncontrolled dissipative processes to the environment. In other words, the initialization takes advantage of the unavoidable energy decay of the circuit, which during the computation is considered a major issue. [35] This decoherence is one of the hurdles of superconducting qubits in general, and poses a dilemma: as decoherence times are increased to allow for more computational power, how to reset reliably and fast to keep the computation cycles fast. One solution, as presented in [35], is to engineer a highly dissipative element, such as a low-temperature resistive bath, that can be tunably coupled to the qubit through resonators. By detuning the resonator sufficiently from the qubits natural frequency, the coupling to the bath is turned off and intrinsic decoherence times are reached. However, tuning the resonator to the qubit frequency, the decoherence time can be greatly reduced and the decay to the ground state accelerated. Alternatively, one could measure the qubit, collapsing it to either of the computational states, and rotate the qubit the ground state if the excited state was measured. However, this method is subject to measurement and single-qubit gate errors.

In order to retrieve the end result of quantum computation circuit, the qubit states need be measured. The most common technique used in the measurement of superconducting qubits is the dispersive readout, where the qubit is capacitively coupled to a linear readout resonator, that can be used to probe the quantum mechanical state of the qubit into a classical response read out by external electronics. In the dispersive limit, the resonator is far detuned from the qubit, which suppresses energy transfer between the two oscillators. The coupling does, however, change the bare frequency of the qubit by a constant Lamb shift, induced by vacuum fluctuations in the readout resonator, and an ac-Stark shift, that depends on the number of excitations, i.e. photons, in the resonator. The photon number dependence of the Stark shift can be a source of dephasing (see Sec. 2.4.1) for the qubit, since the photon number fluctuations lead to fluctuations in the qubit frequency. [28]

In the dispersive regime, the qubit induces a state-dependent frequency shift on the resonator, that can be probed with a microwave pulse to reveal information about the qubit state. For example, one can pulse the resonator at the average frequency $\omega_{\text{RO}} = (\omega_r^{|0\rangle} + \omega_r^{|1\rangle})/2$, where $\omega_r^{|0\rangle}$ and $\omega_r^{|1\rangle}$ are the state-dependent resonator frequencies. Then, after the readout pulse has reflected or transmitted from the chip level, the information of the qubit state is encoded in the phase of the signal, and can be recovered through classical signal processing. A key factor in successful qubit readout is to maximize the signal-to-noise ratio and to minimize the potential back-action to the qubit. Higher readout fidelities can be achieved with longer readout pulses, but longer times subject qubits to energy decays governed by their decoherence times. State-of-the-art solutions utilize Purcell filters and parametric amplification in order to increase the signal-to-noise ratio at faster readout times. [28]

2.4 Noise in superconducting qubits

Like any physical system, quantum computers exhibit noise. The delicacy of current physical implementations mean that they are highly susceptible to errors induced by different noise mechanisms. In fact, the noise governs the field to such a degree that the current era has been named the NISQ (noisy intermediate-scale quantum) [9]. Vast resources are being dedicated to design and build less error-prone devices and at the same time new schemes are being discovered to mitigate and even to correct for errors, both in the pursue of fault-tolerant quantum computing. Nevertheless, even the term implies that errors will always occur and need to be managed. The different physical implementations of quantum computing all exhibits similar noise behaviour, especially the characteristics originating from the physics of open quantum systems, but they do have their own nuances. This sections focuses on superconducting qubits, but many of the topics are applicable to other computing schemes as well.

Quantum mechanically noise and control are two sides of the same coin. In order to minimize environmental noise, the coupling between the system of interest and the outside world should be minimized, but at the same time some well-understood coupling is needed to control the system. A concrete example: single qubit control is achieved with coupling to microwave drivelines, but the coupling is a trade-off between control gained and introduction of a possible relaxation processes decreasing the qubit's lifetime [21].

Based on their effect on system dynamics, errors can be grouped into incoherent and coherent errors. Incoherent errors lead to decoherence meaning the loss of quantum information, and are stochastic by nature. On the other hand, coherent errors are systematic and unitary, such as a fixed error in control pulses, and can often be canceled by better calibration. The coherence is preserved, but the state or the process no longer match the intended one. Coherent errors scale qaudratically in circuit depth instead of linear scaling of decoherent errors and can therefore be more detrimental to computation, which has inspired ways to transform coherent errors incoherent, such as randomized compiling [36] and quantum measurement emulation [37]. This work focuses on the mitigation of coherent errors with composite sequences, which can also be seen as a transaction between a reduction in coherent control errors and an increase in environmental decoherence due to longer execution times.

This section discusses the standard model for characterizing decoherence with energy relaxation and dephasing, as well as coherent noise and its sources. The concept of fidelity is also discussed as a tool to compare noisy processes against their ideal counterparts. Lastly, ways to implement decoherence and coherent errors into simulation are presented.

2.4.1 Decoherent quantum processes

A two level quantum system can be studied using the Bloch-Redfield [38, 39] model for open quantum systems. In this context the loss of quantum information is characterized by two decay functions and their respectively decay rates: longitudinal and transverse.

The longitudinal relaxation describes the energy relaxation of the qubit, and it is expressed with a relaxation rate Γ_1. It originates from an x- or y-axis coupling to the environment, which relates to the fact that the off-diagonal elements in the interaction Hamiltonian drive the excitation and relaxation between $|0\rangle$ and $|1\rangle$. The overall rate can be expressed as a sum of the excitation and relaxation rates $\Gamma_1 = \Gamma_{1\uparrow} + \Gamma_{1\downarrow} \equiv 1/T_1$, where the longitudinal relaxation time T_1 is also introduced as a characteristic $1/e$ decay time scale in which the steady state is reached. The "up" and "down" rates satisfy the detailed balance $\Gamma_{1\uparrow} = \exp(-\hbar\omega/k_b T)\Gamma_{1\downarrow}$. In the regime of typical superconducting qubits with frequencies $\omega_\mathrm{q}/2\pi \approx 5\,\mathrm{GHz}$ at millikelvin temperatures the excitation rate is exponentially suppressed and the qubit tends to relax to the ground state. Also, the qubit transitions are only driven on a narrow frequency band at the qubit frequency.[28] This means that Γ_1 is only affected on that narrow band, where the noise power spectral density is constant resulting in white noise. This also relates to vanishing correlation times and thus the Markovian assumption of an exponential decay holds well.

The decoherence of a superposition state is described by the transverse relaxation rate Γ_2, and it is mediated by both longitudinal (z-axis) and transverse (x-y plane) noise. As discussed above, the longitudinal relaxation rate Γ_1 tends to relax any state into the ground state. Moreover, this leads to loss of the phase information of the state; when a superposition state $(|0\rangle + |1\rangle)/\sqrt{2}$ relaxes to $|0\rangle$, the original location on the equator of the Bloch sphere is no longer evident. Transverse noise causes the qubit frequency to fluctuate, which leads to dephasing, characterized by the dephasing time Γ_ϕ. The effect is stochastic in nature, but since no energy is exchanged with the surrounding environment, the process could be reversed, e.g. with dynamical decoupling [40]. Also, pure dephasing is mediated by broadband noise, since the qubit frequency can be shifted by noise at all frequencies. The effective rate combining both noise mechanisms is

$$\Gamma_2 = \Gamma_1/2 + \Gamma_\phi, \tag{53}$$

assuming that dephasing is generated by Markovian processes. [28]

In superconducting qubits, the general noise spectrum tends to have $1/f$ spectrum, meaning noise is biased to low frequencies. This nuisance, also know as flicker or pink noise, often originates from unknown or uncontrollable changes in the studied system or it's control and measurement electronics [27]. The low frequencies translate to long correlation between noise events exceeding the time scales related to the computational operations on the circuit. As mentioned earlier, energy relaxation is only driven on a narrow band at the qubit frequency, and therefore T_1 is unaffected by $1/f$ noise. However, the low frequency noise does induce pure dephasing. This non-Markovianity breaks the exponential Bloch-Redfield assumption of the pure dephasing decay function and thus the characteristic decay time T_2 cannot be calculated as in Eq. (53). In the interest of having a simple and well-established benchmark for transverse relaxation, the exponential decay model is still used, and it is a reasonable approximation when $T_\phi \gtrsim T_1$ [28]. For physical implementation it is typical to aim for a T_2 limited by T_1 through the theoretical limit $T_2 < 2T_1$ as pure dephasing vanishes [40], which would reinforce the approximation.

2.4.2 Fidelity

The similarity of two quantum mechanical states can be estimated by their fidelity. In the field of quantum computing it is the de facto measurement for the accuracy of the computation, but it does have some variations in the definitions and applications. However, a well established standard is given in Ref. [1], where the fidelity between density matrices ρ and σ is defined as

$$F(\rho,\sigma) \equiv \mathrm{tr}\sqrt{\rho^{1/2}\sigma\rho^{1/2}}. \tag{54}$$

It is not truly a metric, but does have many other suitable features. Firstly, its values are bounded between 0 and 1, $0 \leq F(\rho,\sigma) \leq 1$, with the upper limit met only if the states are identical, i.e. $\rho = \sigma$. Also, $F(\rho,\sigma) = 0$ only if ρ and σ have support on orthogonal subspaces and are thus perfectly distinguishable. Furthermore, it is symmetric with respect to the inputs, $F(\rho,\sigma) = F(\sigma,\rho)$. If either of the states is pure with a density matrix is given by $\rho = |\psi\rangle\langle\psi|$, Eq. (54) simplifies to

$$F(|\psi\rangle,\sigma) = \mathrm{Tr}\sqrt{|\psi\rangle\langle\psi|\,\sigma\,|\psi\rangle\langle\psi|} = \sqrt{\langle\psi|\,\sigma\,|\psi\rangle}\mathrm{Tr}\sqrt{|\psi\rangle\langle\psi|} = \sqrt{\langle\psi|\,\sigma\,|\psi\rangle}, \tag{55}$$

where the properties of pure states $\rho = \rho^2$, and $\mathrm{Tr}(\rho) = 1$ were used. The square of the fidelity introduced in Eq. (54) was originally proposed as the definition of fidelity by Jozsa [41], and the two are at times used ambiguously in literature, with Eq. (54) naturally yielding superior values.

As the states in computational quantum systems are often achieved by applying an engineered quantum process, it is practical to introduce the concept of process fidelity $F_{\mathrm{pro}}(\mathcal{E},\mathcal{F}) \equiv F(\rho_{\mathcal{E}},\rho_{\mathcal{F}})$, where $\rho_{\mathcal{E}}$ and $\rho_{\mathcal{F}}$ are the states created by the processes $\mathcal{E}$ and $\mathcal{F}$. When one of the channel is unitary, e.g $\mathcal{F} = U$, as frequently is the case when comparing physical implementation to ideal evolution, the process fidelity can be expressed using the superoperator description of quantum channels (see Sec. 2.1) as

$$F_{\text{pro}}(\mathcal{E}, U) = \frac{\text{tr}(\mathcal{L}_U^\dagger \mathcal{L}_\mathcal{E})}{d^2}, \tag{56}$$

where d is the dimensionality of the channels [42]. Moreover, the fidelity of a quantum process can depend on the initial state of the system, and in order to capture the full dynamics, the average fidelity is defined as

$$F_{\text{ave}}(\mathcal{E}, \mathcal{F}) \equiv \int d\psi F(\mathcal{E}(\psi), \mathcal{F}(\psi)), \tag{57}$$

where the integration is done over the state space. Again, for a unitary channel $\mathcal{F} = U$ this simplifies to [43, 44]

$$F_{\text{ave}}(\mathcal{E}, U) = \frac{F_{\text{pro}}(\mathcal{E}, U)d + 1}{d + 1}. \tag{58}$$

For a analytically defined quantum processes used in simulations, Eqs. (56) and (58) provide an efficient way to calculate the average fidelity. However, in physical quantum computers the actual quantum channel is not fully known, so neither are their superoperators. This gives rise to a need for an experimental method to evaluate the same fidelity definition. An immediate solutions would be to estimate the channel using quantum process tomography, but it scales unfavorably, as $d^4 - d^2$ observable average measurements are needed for d dimensional quantum channel [1]. However, there does exist alternatives that alleviate part of the computational cost [43].

2.4.3 The simulation of noise and errors

The longitudinal and transverse decay functions within the Bloch-Redfield model are easily integrated to the Lindblad model to analyse open system evolution. The longitudinal energy relaxation is described by an collapse operator $a/\sqrt{T_1}$, where a is the annihilation operator. Similarly, the transverse decay is defined as $a^\dagger a\sqrt{2/T_\phi}$. [45] The time-evolution can then determined by numerically solving the differential equation, of course keeping in mind the assumptions made both in the Bloch-Redfield model and the Lindblad master equation.

The simulation of coherent errors is more straightforward. Based on the level the system is described in the simulation, systematic errors can be introduced in many ways. For example, if a transmon qubit is designed for some target frequency and anharmonicity, the physical device will always differ from these values. A systematic error could then be attributed to either the frequencies directly, or to the underlying parameters, e.g. physical size or material constant. The control of qubits is subject to comparable errors, since the capacitive coupling between the qubit and the driveline is also affected by deviation from design parameters. Moreover, the electronic signals controlling the magnetic flux in tunable qubits and the control pulses are limited in accuracy. In the perfect world of simulations however, arbitrary control pulses can be created, for example, to create a rotation deviating from the ideal one simply by varying the integral of the envelope function in Eq. (52). The phase of the pulse can also be offset by an user-defined value. It is noteworthy that these same paths can be taken to implement stochastic errors in pulses.

Physical superconducting qubits never truly are two-level system, which can be painfully obvious in weakly anharmonic transmons. The devices experience leakage errors, meaning state population leaks away from computational subspace to higher excitation states. These higher states can be included in the simulation by defining the system Hamiltonian with general creation and annihilation operators in a Hilbert space of the wanted size, instead of the Pauli matrices, as is done throughout this work. However, each additional state grows the computational requirements exponentially.

Lastly, the Hamiltonian can be made to include the dynamics introduced by noise sources including specific interactions with environment and variation in the control field. These further provide methods to use simulation to validate the system's the design, to investigate error budgeting, and to gain new insight about the quantum mechanical system.

2.5 Composite pulse sequences

In principle, a known systematic error can always mitigated with calibration of the qubit system and its controls. However, this is often a tedious task as the initial calibration of a state-of-the-art superconducting quantum processor is time-consuming and the systems need to be regularly monitored for drift and recalibrated. Composite sequences promises to mitigate systematic gate errors up to an arbitrary accuracy by utilising symmetries in the rotation angles of the sequences. These methods have been used in nuclear magnetic resonance (NMR) experiments and applications, where, for example, the dispersion in a large ensemble of quantum system causes unwanted dynamics under a uniform control field. A typical task is to excite a spin ensemble with varying parameters from a initial state to a desired final state. In the spin systems of NMR experiments and applications, possible deviations in parameters include Larmor dispersion, i.e. variation in the precession frequency around an external field, variation in spin relaxation rates and fluctuation in the applied radio frequency control field. Compensating pulse sequences aim to compensate for these dispersions.[11]

Composite pulse sequences has previously been shown to follow the theoretically predicted excitation profiles on superconducting qubits. For example, in 2022 Torosov and Vitanov [13] executed composite pulses on an open access IBM quantum processor and found excellent agreement also with higher order corrections, contributed to the quality of IBM devices and the error mitigation power of these methods. However, how well can composite pulses be incorporated into full-scale computation is still an open scientific question.

2.5.1 Composite sequence classes

Levitt [46] introduces a classification of different composite pulses into types A and B. Type A includes the fully-compensating pulses, meaning the sequences which are not initial state dependent and which transform an initial state into an ideal final state over some range of control. On the other hand type B sequences are called partially compensating, since the transformation does not fully achieve the ideal one. Subtypes of this group include sequences up to a phase shift (B1), initial state dependent sequences (B2) and the combination of both conditions (B3). In the framework of quantum computing, type B sequences are of little use since they require information about the initial and final states of the operations [47]. Typical computation schemes consist of multiple of these operations and the intermediate states of the system are not stored. Also, the phase of the qubit is a highly valuable asset. Considerable efforts are taken to mitigate the dephasing of qubit systems (see Sec. 2.4.1), and phase shift inducing sequences would quickly make these efforts futile.

In the NMR literature, an ideal unitary transformation is often denoted as θ_φ, which translates to [48]

$$U(\theta,\varphi) = \exp[-i\theta(\sigma_x \cos\varphi + \sigma_y \sin\varphi)]. \tag{59}$$

With the difference of a factor of half for θ, this is identical to transformation created by the PRX gate (Eq. 17). However, the real physical system has finite errors and the above transformation is never accurately reproduced. By assuming a fractional error f in the angle θ, the real transformation can be described as

$$V(\theta, \varphi) = \exp[-i(1+f)\theta(\sigma_x \cos\varphi + \sigma_y \sin\varphi)], \tag{60}$$

The previous assumes a linear error model. A model that captures the error as a factor in the rotation angle is applicable to pulse amplitude and pulse length errors, since they have a similar effect in the integration over the pulse shape. However they arise from different physical mechanisms [47]. The exact size of error does not need to be known, as long as it in a certain correctable window, but it is however necessary to know its form [48].

The pulse sequences can also be categorized based on whether they search for a new sequence that achieves the target transformation with a favorable error susceptibility, or whether they aim to cancel the error caused by the application of original gate after the fact. Below we introduce composite pulse sequences of both kinds, the SCROFULOUS and the BB1 sequences.

2.5.2 SCROFULOUS sequence

The SCROFULOUS (Short Composite ROtation For Undoing Length Over and Under Shoot) pulse sequence originates from the field of NMR and was initially derived to compensate for pulse length errors. It is based on the work by Tycko *et al.* [49] from 1985, where $\pi/2$ and π-rotations robust against phase shifts were studied, at a time when the shortcomings of type B1 sequences was already recognised. It was later generalized and named by Cummings, Llewellyn and Jones [14] in 2003. The original three pulse sequence for a nominal $180^\circ_{0^\circ}$ rotation around x-axis is given as

$$180^\circ_{60^\circ}180^\circ_{300^\circ}180^\circ_{60^\circ}. \tag{61}$$

Further analysis, which falls outside the scope of this thesis, reveals, that a three part pulse sequence correcting errors in the first order can be constructed as

$$\theta_{1\varphi_1}180^\circ{}_{\varphi_2}\theta_{3\varphi_3}, \tag{62}$$

with

$$\begin{aligned}\theta_1 = \theta_3 =& \text{arcsinc}\left(\frac{2\cos(\theta/2)}{\pi}\right)\\ \theta_2 =& \pi\\ \varphi_1 = \varphi_3 =& \arccos\left(\frac{-\pi\cos\theta_1}{2\theta_1\sin(\theta/2)}\right)\\ \varphi_2 =& \varphi_1 - \arccos(-\pi/2\theta_1),\end{aligned} \tag{63}$$

where $\text{sinc}(x) = \sin(x)/x$ and θ is the nominal rotation. The intended angle θ is kept as a variable, and again, the phase angle can be tuned by offsetting all of the φ_i angles by the wanted amount. The angle definitions above yield a time-symmetric sequence. A quantum circuit recreating an error-tolerant PRX(π,0) gate is then

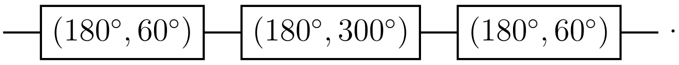

2.5.3 BB1 sequence

In 1994 Stephen Wimperis [15] introduced a wide range of fully compensating composite pulses in the NMR context, categorized to broadband, narrowband, and passband pulses. In the context of quantum computing, the broadband pulses, which originally intended to compensate for errors induced by unhomogenous radiofrequency fields, have gained the most attraction. The radiofrequency unhomogeneity is comparable to an error in the qubit control, in that a broadband sequence would more closely achieve the ideal unitary transformation over a larger coherent error range. However, narrow band pulses, which drive excitations on a narrower range compared to bare pulses, could have applications on addressing detuned neighbouring qubits [13]. Passband pulses aim to combine robust control near the target frequency with sharp transitions to suppressed excitations.

From the pulses introduced by Wimperis, the BB1 (for the simplest broadband pulse, not to be confused with type B1) has been popular. It is a fully compensating pulse sequence, that is able to correct for errors up to the second order [14]. A operations of θ_φ is replaced by a sequence of four gates:

$$\text{BB1}(\theta) : 180^\circ_{\varphi_1} 360^\circ_{\varphi_2} 180^\circ_{\varphi_1} \theta_{0^\circ}, \tag{64}$$

with $\varphi_1 = \arccos(-\theta/720°)$ and $\varphi_2 = 3\varphi_1$. As the gates commute, a time-symmetric equivalent can be created with an expense of one additional physical gate:

$$(\theta/2)_{0°}180°_{\varphi_1}360°_{\varphi_2}180°_{\varphi_1}(\theta/2)_{0°}. \tag{65}$$

In the quantum circuit notation a single PRX$(\pi, 0)$ gate, a π-rotation around the x-axis, would be transformed approximately to

$$-\boxed{(90°, 0°)}-\boxed{(180°, 104.5°)}-\boxed{(360°, 313.4°)}-\boxed{(180°, 104.5°)}-\boxed{(90°, 0°)}- \;.$$

The BB1 pulse, as well as the other sequences proposed by Wimperis, has also been extended to correct error to an arbitrary order $O(f^n)$, where f is the error, in contrast to the third order correction of simplest sequence [50]. While higher order corrections would theoretically yield more accurate operations, the number of gates needed to perform these corrections grows rapidly and the advantage would quickly be overcome by decoherence. Other arbitrarily accurate pulses suffering from the same drawback have also been presented [51].

3 Methods and materials

3.1 Simulation tools

3.1.1 Atos Quantum Learning Machine

The Quantum Learning Machine (QLM) [52] is a full-stack simulation tool for quantum information processing build and developed by Atos, a global corporation working across the digital sector. It provides a Python software library for the development of quantum circuits and algorithms, and the tools to incorporate physical details, such as topology, native gates, and noise models into the simulation. The computation is done on a purpose-build server, one of which is hosted and operated by CSC [53], a Finnish non-profit state enterprise, and it can accessed remotely as part of their service portfolio.

QLM is the first of the two simulators used in this work. Admittedly, the software and hardware capabilities go way beyond the scope needed for simulating single qubit unitary gates with a standard Bloch-Redfield noise model. However, the fidelity landscape measurements, reported in Sec. 4.1, do start to take advantage of the computational resources. As a downside QLM does rely on qubits truly being two-level systems without higher excitation levels, and essentially computes the evolution by multiplying matrices in the dimensions of the system. Most often this is sufficient for testing and development on the algorithm level, however a more detailed simulator could reveal dynamics not captured by the simple model in QLM.

3.1.2 Pulse-level simulation with Qutip-qip

The second simulator works on the so-called pulse-level. It introduces a more physically accurate description of a superconducting qubit system at the cost of increased computational resources. In pulse-level simulation the time-dependent system Hamiltonian is defined and the initial state is evolved numerically by the Schrödinger equation in the case of a coherent, closed system. The open system dynamics can also be easily incorporated with collapse operators, e.g. as discussed for the Bloch-Redfield model in Sec. 2.4.3, and in that case the Lindblad master equation in (10) dictates the system's time evolution. The Hamiltonian includes terms both independent and dependent on time, and the qubit control terms are part of the latter. The dynamics of real superconducting qubits can be investigated by pulsing the control terms. Also, since the Hamiltonian can be defined with general ladder operators instead of two-level Pauli matrices, the higher excitation levels can be included to the simulation. Different pulsing methods, such as the DRAG scheme, can also be investigated. The inclusion of the second excited state, i.e. simulating the system as qutrits, can give new insight about leakage errors caused by population transfer out of the computational subspace. This model naturally exponentially increase the computational cost, since the density matrix grows from 2×2 to 3×3. However, in weakly anharmonic transmon this can be quite strongly motivated.

The aforementioned details are included in an open-source Python library called Qutip-qip, formerly part of larger Qutip library [54] for general quantum mechanical open system simulations, but has since been spawned into a more tailored sublibrary using the conventions of QIP. It was introduced with examples in Ref. [45]. Mainly, it provides an interface between the gate-level abstraction and the quantum mechanical physics in the quantum computer, and is thus a promising candidate for more accurate simulation that still takes quantum circuits as an input. As such it also nicely meets the requirements for this work. The accuracy of the simulation is dependent on the Hamiltonian defined, which also opens up a possibility for introducing more complex interactions. The simulation is made physically relevant by taking experimental values, such as qubit frequencies and anharmonicities, drive parameters and decoherence times, as input. The time evolution is solved by using Qutip's master equation numerical solver.

Qutip-qip also provides predefined classes for different quantum computer realisations. The Processor class works as the main interface between the circuit-level description and the open system numerical calculations, while the Model describes the system Hamiltonian with relevant parameters that are passed to the numerical solver. Taking inspiration from their SCQubits class, we inherit from both classes and modify the children to follow IQM's technological details. The system Hamiltonian is described in the rotating frame by a Duffing oscillator driven on-resonance with the rotating wave approximation applied (Eq. 49).

3.2 IQM Quantum Processing Unit

To investigate the true error mitigation capability of SCROFULOUS and BB1 pulses, a 5-qubit quantum computing processor (QPU), build and operated by IQM, was deployed. The QPU has a star-shaped topology, with a central transmon connected to four other transmons via tunable couplers. The central qubit was used for the experiment, with measured decoherence times $T_1 = (32 \pm 1)\,\mu\text{s}$ and $T_2 = (37 \pm 2)\,\mu\text{s}$. The average fidelity of a single-qubit gate, with a duration of 40 ns, of over 99.9 % was confirmed using randomised benchmarking. The transmon had a frequency of 4.118 GHz and an anharmonicity of -219 MHz. The above mentioned values were used in the pulse-level QPU simulation. Also, a Gaussian DRAG pulse was used for the gates both in simulation and on the QPU. A single shot readout fidelity of 94.9% was measured for the qubit in use, with the excited state falsely measured as ground 6.2 % of the times, and the ground state measured as excited 3 % of the times. These are denoted as $P_{e\to g}$ and $P_{g\to e}$ respectively. The measurement error mechanisms are not included in the simulations, but a simple correction can be made to the probabilities of the ground and excited states. For example, the corrected excited state probability P_e can be calculated from the simulated probabilities P_e^{sim} and P_g^{sim} with $P_e = P_e^{\text{sim}}(1 - P_{e\to g}) + P_g^{\text{sim}} P_{g\to e}$.

In the experiments each circuit was repeated $m = 2000$ times to get a statistical average of the measurement outcome. In the situation were the excited state is measured, each measurement yields $z_i \in \{0,1\}$, and the mean can be calculated as $\sum z_i/m$. For large m the distribution becomes Gaussian and, using the central limit theorem, the mean represents the true value for the probability. The standard deviation is $\Delta z/\sqrt{m}$, where Δz is the standard deviation for a single measurement, that is bounded to be lower than 1/2. The standard deviation is then at most $1/\sqrt{4m}$. [1]

4 Results

4.1 Characterising the sequences with QLM

The composite sequences promise to cancel systematic rotation errors with increased gate numbers relating directly to increased computation time. The interplay between systematic coherent error and decoherence caused by the longer processes was investigated by sweeping the error and the gate time, and calculating the average gate fidelities (Eq. 58) for the respective two-level quantum channels in QLM. The ideal gate was chosen as a π-rotation about the x-axis. The qubit specific decoherence times of $T_1 = 32\,\mu\mathrm{s}$ and $T_2 = 37\,\mu\mathrm{s}$ were used to create noisy quantum channels as discussed in Sec. 2.4.3. However, using the fundamental limit of $T_2 = 2T_1$ has only a small effect in the fidelities. The resulting fidelity landscapes are shown in Fig. 4, with a hundred equidistantly spaced values used for both variables. On the horizontal axis the gate time is divided by the constant T_1, and the scale is chosen to represent the state-of-art regime for T_{gate}/T_1 ratio in superconducting qubits.

The fidelity improvements of the SCROFULOUS and BB1 sequences over the native gate are seen in Fig 4a and Fig 4b, respectively. The results are fairly similar. To begin with, these results suggest that a fairly large systematic error is needed to find substantial benefits from these sequences. At $T_{\mathrm{gate}}/T_1 = 10^{-3}$ the threshold for a gain is crossed at low single digits errors, and when the ratio decreases close to 10^{-4} a benefit can be seen at smaller errors. In Fig. 4c the sequences are compared to each other qualitatively. The SCROFULOUS pulse reaches higher fidelities at smaller errors, but the switching point increases with the gate time. BB1 is capable of correcting larger errors, as stated in literature [14]. The two additional gates in comparison to SCROFULOUS do lead to more decoherence, but this effects becomes negligible as gate time decreases, hence the funnel-like shape of the data. Since ideal rotation is achieved with both sequences at the limit of zero error, BB1 would be the obvious choice at infinite decoherence times. With realistic decoherence values, SCROFULOUS is speculated to be a better candidate.

To conclude, larger fidelity benefits are probably not found in physical devices,

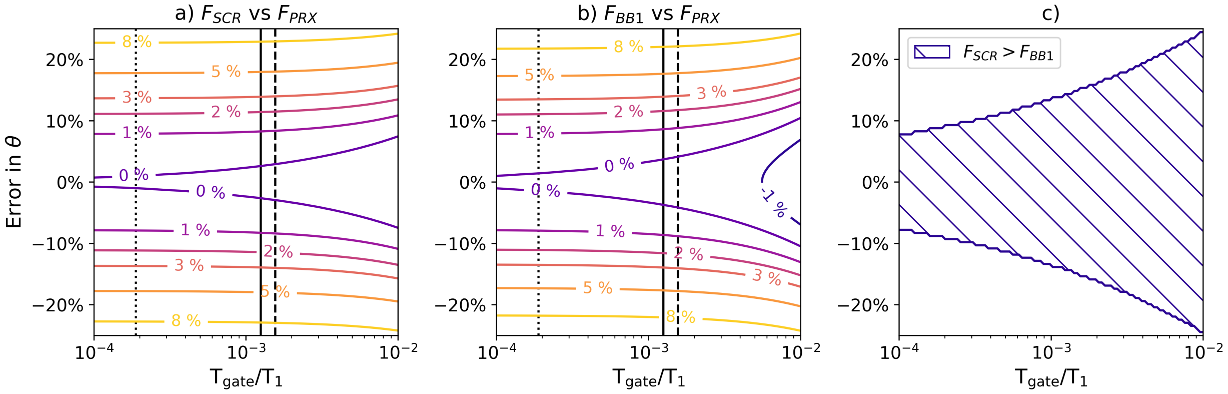

Figure 4. Fidelity comparison of a π-rotation about the x-axis created with a) SCROFULOUS and b) BB1 sequences against the native gate, as a function of T_{gate}/T_1 and error in rotation angle θ, simulated using noisy two-level system quantum channels in QLM, where experimental decoherence values for T_1 and T_2 were used. The contours show the average gate fidelity improvement in comparison to a single native PRX-gate. For reference, the vertical lines indicate T_{gate}/T_1 ratios for the IQM transmon device used in this work (solid), a recent IBM device [55] (dotted), and Google's Sycamore chip during the quantum advantage experiment [56] (dashed). The sequence fidelities are qualitatively compared to each other in c).

since they would require large systematic errors at relevant T_{gate}/T_1 values, which are easily corrected with calibration, but some improvements could be found. Therefore, these results indicate that the sequences, especially SCROFULOUS, could be used to offer some protection against systematic errors as the field works to achieve single-qubit gate fidelities ever closer to unity.

4.2 Transition probability at a wider range

The error correction capability of the methods in this work can be investigated by artificially creating faulty quantum operations. Since only coherent errors are addressed, adding an error to the rotation angle is equivalent to inaccurate calibration at the pulse-level. Additional calibration error could still remain in the execution.

The plotted lines in Fig. 5 represent the ideal unitary results for the sequences for a varying degree of artificially added rotation error. The simulations were performed in Qiskit by building a single qubit circuit starting in ground state and adding the respective gate(s) with a systematic error added to rotation angle, as defined in Eq. (60). The build-in state vector simulator was use to propagate the circuits in the

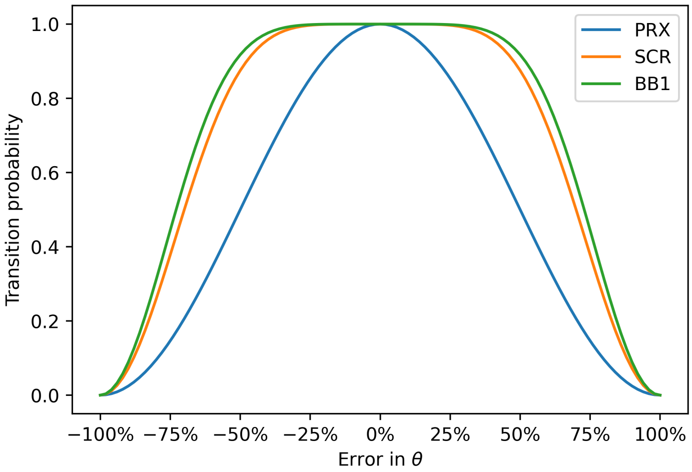

Figure 5. The results for measuring the excited state after applying a single gate or one of the two sequences to the ground state, for a varying degree of artificially added rotation error. The lines represent ideal, unitary simulations of the respective circuits without decoherence.

unitary case and the probability amplitudes for the excited states were read from the results and squared. For the single-qubit gate, the expected sinusoidal behaviour can be identified. This can be related to the Rabi oscillations in a resonantly driven two-level system. As expected [14], BB1 corrects errors in a slightly wider range compared to SCROFULOUS, a characteristic also identified in the previous Sec. 4.1. This is also a consequence of SCROFULOUS and BB1 correcting errors in the first and second order, respectively. However, with errors ranging from roughly -25 to 25 %, both sequences perform almost identically. The sequences match the native gate at 0 %.

To gain more insight into how composite pulse sequences perform on a superconducting quantum computer, they were simulated on the pulse-level simulator and run on the IQM quantum processing unit. Figures 6 shows (a,d) the single qubit PRX gate, (b,e) SCROFULOUS and (c,f) BB1 on a physical qubit compared against simulation. As above, the transition probability from ground to excited state is plotted with respect to artificially added rotation error. The readout fidelity corrections were made to the simulation results, and the errors displayed are the standard deviations over 2000 samples (see Sec. 3.2). The results show that probabilities are slightly lower than the simulations would suggest throughout the error range. This is most likely due to noise that is not captured by simulation setup. The sequences

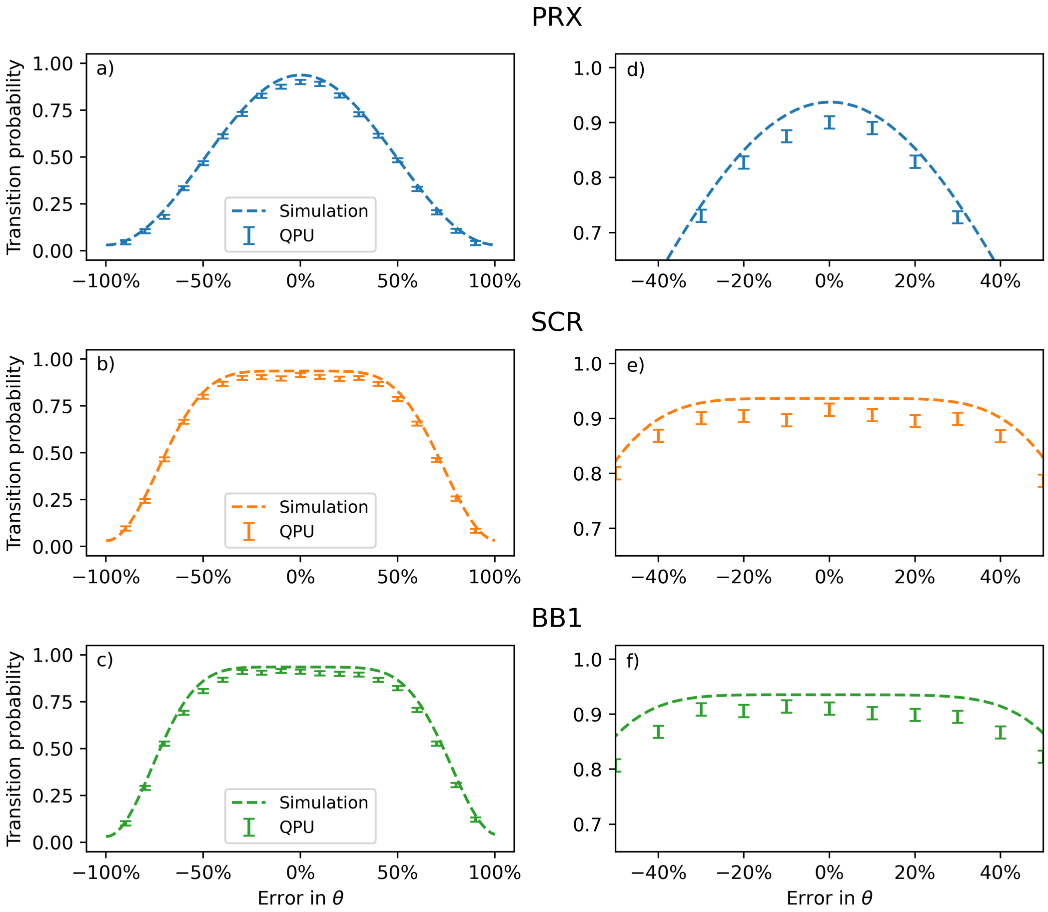

Figure 6. Transition probability from ground to excited state with the native PRX($\pi, 0$) gate (a,d), SCROFULOUS (b,e), and BB1 (c,f) on an IQM QPU compared against noisy three-level simulations with Qutip-qip. Artificially added rotation error in the -100 to 100 % range were added for each method.

take longer to execute, by factors of three and five for SCROFULOUS and BB1, respectively, but this should have a minimal effect since the gate time is three orders of magnitude smaller compared to the decoherence times. At the point where no artificial error is added (0% on horizontal axis), one would expect all three methods to achieve similar probabilities, and this is confirmed by the results. The exact values are 0,901 ± 0,012, 0,916 ± 0,012 and 0,911 ± 0,012 for PRX, SCROFULOUS and BB1, respectively. This could be interpreted as the sequences correcting for a small unknown amplitude error, but the uncertainties overlap to the extent that this is advised against.

In general, the composite sequences behave as expected and as previously reported in literature for superconducting qubits [13]. The QPU results also match reasonably well with the simulations, giving some reassurance about the accuracy of the pulse-level simulator. Systematic errors ranging from about -25 to 25 % in the rotation angle are well corrected. However, such large errors are typically eliminated in the calibration procedure, and the question whether these methods could be used to mitigate the remaining errors is not yet answered.

4.3 Repeated π-rotations

Next, the investigation proceeds into repeated rotations. While not strictly needed for gate-based universal quantum computing, since all consecutive single qubit operations can always be compiled to an effective operation, it is a commonly used technique in error calibration (for a recent example see [57]). In the calibration of single qubit drive amplitude it can be used to fine tune the amplitude value gained from a Rabi oscillation experiment, since the error is amplified in consecutive pulses.

In the experiment each circuit starts with a PRX($\pi/2$,0) gate, initialising the qubit approximately in state $(|0\rangle - i\,|1\rangle)/\sqrt{2}$, with the state vector pointing along the negative y-axis in the Bloch sphere picture. Measuring the initial state should then reveal equal population in both ground and excited states. This is done in order for the subsequent errors in state population to be linearly dependent on the systematic error of the π-rotation or corresponding sequences. Then, π-rotations are repeated and the population should ideally remain constant after each addition. In the simulation in total 20 rotations were performed at most, and this number was increased to 48 on real hardware. Additionally, the rotations are added in pairs to cancel out oscillations in the population.

Again, the pulse-level simulation with the Bloch-Redfield decoherence model was deployed. Figure 7a shows simulated results for the experiment in the case of the native gate. The error-free gate is compared to few artificially faulty ones. As expected, adding larger errors causes the probability to measure the excited state to increase as functions of the amount of error and the number of rotations. The plot closely resembles a typical output of a calibration experiment. The initial offsets from 0.5 is due to equal error in the initialisation gate, but they decrease for larger artificial errors. The results also reveal that the single-qubit gate as implemented in the Qutip-qip simulator does have an intrinsic rotation error, that is captured by the decreasing probability in the 0 % error case. It can be extrapolated that the nominal π-rotation under-rotates the state by a few parts per thousand. To investigate the

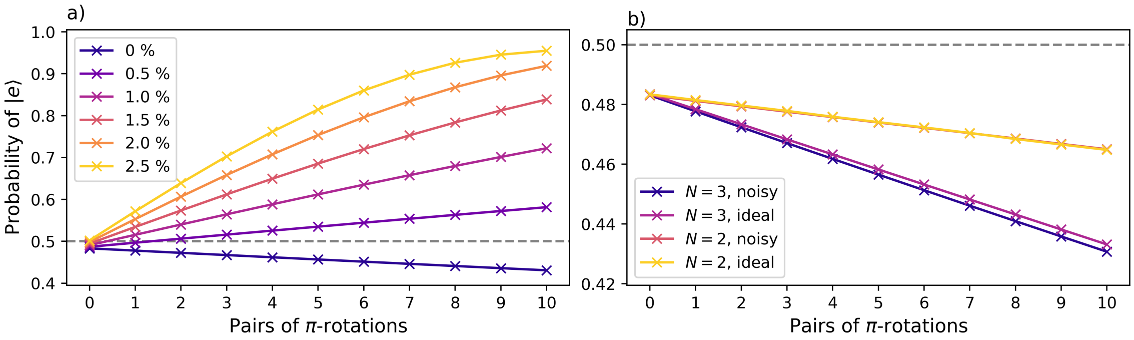

Figure 7. Pulse-level simulation results for the probabilities to measure the excited state $|e\rangle$, when starting in an equal superposition on the negative y-axis and applying repeated pairs of π-rotations around the x-axis, plotted with a few values for the amount of error in the rotation angle. An unintentional coherent error is seen the 0 % case and in b) this is plotted for two and three-dimensional systems with and without Bloch-Redfield decoherence model. For $N = 2$ the noisy and ideal results are very close and overlaid in the plot.

origin of this effect, the 0 % error gate was simulated using both two and three-level systems with and without decoherence. From the results in Fig. 7b one can attribute a large part of the error to leakage to the second excited state, since the error is clearly reduced when limiting system dimensions, and that decoherence has little significance. The remaining error is most likely due to bad parameters or numerical errors in the simulation model.

Figure 8 extends the simulation analysis to the sequences, as the earlier result of the native gate is compared against SCROFULOUS and BB1. Firstly, the SCROFULOUS sequence shows excellent performance in keeping the population constant, emphasising its potential as an error mitigation tool. However, the same does not apply to the BB1 sequence; for unknown reasons the population drifts towards the excited state. The drift is not affected by the amount of error at least in the range chosen. After careful examination of the simulation setup and confirmation of the gate arguments, a concrete reason for the behaviour is not found.

The same experiment was conducted on real hardware, and the results are shown in Fig. 9. Most notably, the native single-qubit gate is able to keep the probability stable, when compared against the sequences. For the BB1 sequence, the probability drifts towards the excited state, as it did in the simulation. The amount by which the population drifts over ten pairs is also comparable: about 10 %. On the other hand, for SCROFULOUS the probability drifts towards the ground state, and this

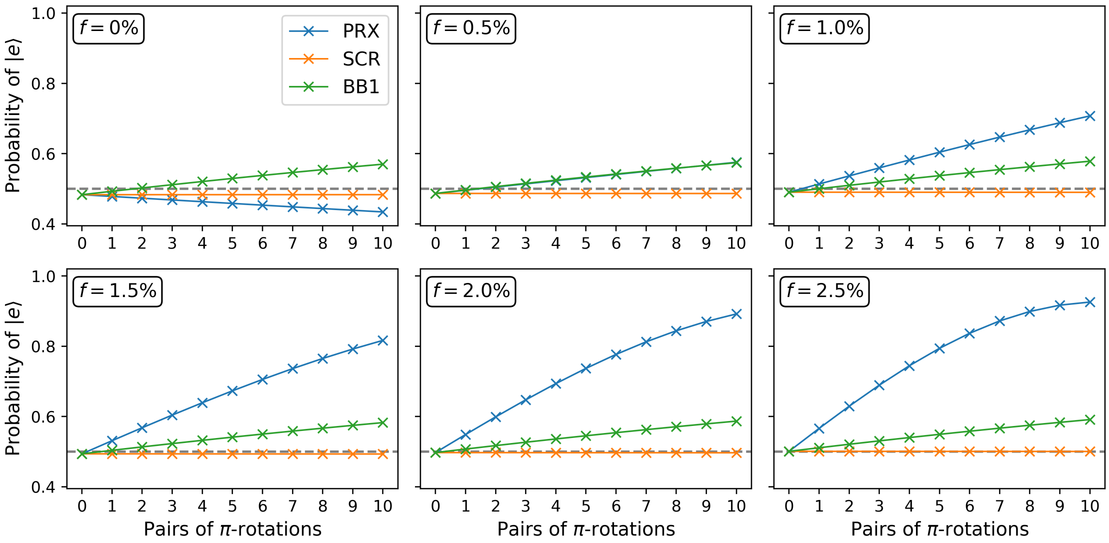

Figure 8. Extending from the pulse-level simulation of Fig. 7, the accumulation of error is visualised by plotting the probability of excited state $|e\rangle$ as a function of pairs of π-rotations. The sequences show similar performance in all cases, accounting for the error in initialisation. SCROFULOUS corrects errors reliably, while BB1 drifts from equal population irrespective of the amount of error. PRX and BB1 data points are practically identical in the $f = 0.5\%$ case.

effect was not seen in the simulations. Therefore, it could be speculated, that the reasons behind these effects are at least partly separate, because only BB1 drifts in the simulations. Furthermore, the initialisation is imperfect, as the probabilities start below 0.5 in all three cases. The uncertainties represent the standard deviation over 2000 samples. To conclude, the native gate seems to be the most accurate during repeated π-rotation, and the sequences perform miserably. While previously all three methods have been assumed to perform equally in the limit of very small errors, it could be speculated that in this regime the native gate is more accurate, and that there is a threshold for the magnitude of the fractional error after which the sequences become more accurate. Such an effect was left as a possibility in Sec. 4.2. Unlike in Sec. 4.1, the effect would not be due to lesser energy decay during the single gate, but inaccuracy in physically creating the sequence pulses. However, analytically the sequences converge to the native gate in the small error limit.

As mentioned in Sec. 2.5.3, the BB1 sequence can be expressed as either a time-symmetric sequence with the correcting pulses placed in the middle of the execution, or the correcting pulses can be placed on either side of the original pulse. The resulting overall operators are identical, but keeping the original pulse intact

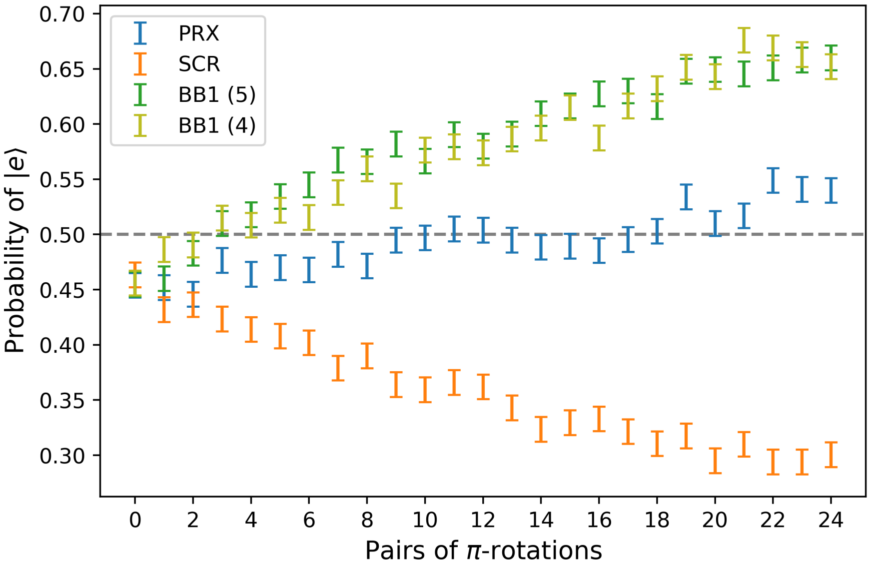

Figure 9. The probability of to measure the excited state as a function of pairs of consecutive π-rotations, executed on an IQM quantum computer for the native single-qubit gate, SCROFULOUS and BB1 sequences. BB1 (5) and BB1 (4) refer to the five and four-gate variants.

saves one pulse, reducing the overhead in the execution time to a factor of four. While the five-pulse sequence have been used through these experiments, here a four-pulse variant, with the correcting pulses placed after the original pulse, was also experimented with. The results in Fig. 9 reveal that the sequences perform similarly.

As the execution times increase, the decoherence effects become more significant. Rough estimates for the intrinsic energy relaxation can be made in the two-level Bloch-Redfield noise model. For the native gate the longest execution time was $(1+48) \times 40$ ns $= 1960$ ns, during which the excited state probability decreases by a factor of $\exp(-1960\,\mathrm{ns}/32\,\mu\mathrm{s}) \approx 0.94$. Due to the overhead in execution times, for SCROFULOUS and BB1 with five gates the factors are 0.83 and 0.74, respectively. Therefore the energy relaxation should be taken into account when considering the results of Fig. 9. For example, removing T_1 decay in this simplified way from the probability of the last SCROFULOUS data point with 24 pairs of rotations would give roughly $0.3/0.83 \approx 0.36$, and thus still indicates towards a slight downwards slope.

4.4 Process tomography for the sequences

To get a sense on how the sequencing methods perform on an arbitrary initial state, the concept of quantum process tomography (QPT) is introduced. It extends quantum state tomography, a procedure to experimentally determine the unknown quantum state of a system, to determining an unknown quantum process. In the case of single qubit, the system is first prepared in a chosen orthonormal set of the eigenstates for Pauli matrices, then evolved by the process one wants to characterise, and finally measured in the basis determined by the Pauli matrices. This will yield 12 different experiments, and based on the results a quantum channel, which represents the noisy process in the system, can be constructed. The quantum channel representation can then be used to get an estimate for the average gate fidelity irrespective of the initial state. [1]

Here, the characterisation relies on QPT as it is implemented in the Qiskit Experiments Python library [58]. It provides a low overhead approach with existing circuit generation and analysis tools. The output includes a Choi-matrix representation of the quantum channel and its process fidelity, from which an average gate fidelity can be calculated (Eq. 58). The experiment was repeated ten times for the native single-qubit gate, SCROFULOUS and BB1.

Table 1 shows values attained over the ten repetitions. It is clear that QPT fails to characterise the error mitigation methods as it gives almost identical fidelities for all three cases. Also, the native gate value of 0.94 ± 0.010 is substantially smaller than 99.9% reported based on randomised benchmarking. The standard deviations are small, and thus the culprit must be in the procedure itself. Main reason for the discrepancy is that the preparation and observable operations are subject to the same errors and noise as the studied processes, while the derivation and the analysis of QPT assumes them ideal. The readout fidelity of 94.9 % is close to the QPT fidelity estimates achieved here, and thus it seems that possible small differences in the native gate and sequence fidelities are overshadowed by the readout error. Additionally, the preparation and observable operations lengthens the circuit always by two gates, thus disproportionately affecting shorter circuits, which makes the comparison of the achieved values difficult.

The shortcomings of QPT could be addressed by using a self-consistent tomography method called quantum gate set tomography (GST) [59], which accounts also

Method	Average gate fidelity
PRX	0.94 ± 0.010
SCR	0.943 ± 0.005
BB1	0.943 ± 0.012

Table 1. The fidelity data obtained with quantum process tomography on an IQM quantum processing unit.

for the errors in state preparation and observable operations. The superiority of GST as a process characterisation tool is especially advantageous when the fidelities increase near and above the quantum error correction limits. However, GST adds more overhead, with approximately 80 distinct circuits needed for single qubit characterisation and a classical optimisation problem used in the analysis of the result. While acknowledging the shortcomings of QPT and the somewhat meaningless results achieved, the characterisation of the sequences using GST is left as a possible future endeavour.

5 Conclusions

The field of quantum computing is slowly but surely progressing towards larger and more complicated systems. The future promise of quantum advantage might soon become reality. All quantum computers, regardless of the physical implementation, require delicate manipulation of the underlying quantum physical phenomena. In superconducting quantum computers the precise control of the quantum state of a single qubit is one of the fundamental requirements. The present work confirms that composite pulse sequences offer simple and easily compatible solution to the mitigation of large unknown coherent errors in the control pulse amplitude, but fails to find an advantage on the IQM QPU. Therefore, it does not answer the question of how much can be gained over standard calibration practises on superconducting computers in the near term.

Throughout the characterisation full π-rotations with respect to the x-axis are used, even though the sequences are applicable to any single-qubit gate with an arbitrary rotation angle and phase, which are needed for quantum computation. The use of π-rotation does make the analysis of population transfer more straightforward, and it is the largest rotation needed for the state control over the Bloch sphere. Also, the drive amplitude calibration typically involves such pulses, and thus, they could be most accurate on a real device. Smaller rotation angles are often calculated from the calibrated π-pulse, which could lead to larger coherent errors as the control signal attenuates non-linearly through the control electronics. The effect could be reduced by calibrating the signal for a discrete number of smaller rotations, and then extrapolating for an arbitrary angle, but it also is a potential source for the coherent errors this work aimed to mitigate.

Based on the achieved results, it can be concluded that both composite pulse sequences, SCROFULOUS and BB1, can be used to correct for large errors in the pulse amplitude in the control of superconducting transmons. However, the experiments on real hardware indicate that current systems do not benefit from their use in the case of longer circuits. While the broadband error correction over a wide range is an interesting behaviour in itself, it is not relevant for control methods used in modern superconducting quantum computers. Much more essential would be to address small errors still remaining after calibration procedures, but here this is not accomplished. The most probable reason for this is that the controls and their calibration are precise enough, and that the application of the sequences create additional errors in the system. However, there doesn't seem to be any fundamental restriction in term of using pulse sequences on superconducting qubits, but this work demonstrates that finding an advantage from these methods is non-trivial and requires in-depth knowledge of the system. In the context of this thesis, further insight would be gained by studying arbitrary operations with the help of a more detailed tomography method, such as GST.

All composite sequences will by their nature lead to more constituents in the desired operation. If, in the future, a fidelity improvement can be achieved with these methods, it will lead to an interesting trade-off between single gate accuracy and computation time; assuming shorter gates can be less accurately calibrated, the sequence could be used to regain some of the accuracy while keeping the overall length shorter. Of course other error types must also be taken into consideration, such as leakage to higher states that is characteristic for short pulses. Also, the linear scaling of the computation time might be manageable as decoherence times increase.

In this work simulation on both the gate and pulse-level gave valuable insight and were able to predict the behaviour of the single-qubit operations. Discrepancies appeared as the system was evolved for a longer duration with more operations, as noise processes that are not captured in the simulation models start to have noticeable effects. It is known that the two-level gate simulations do not represent accurately the dynamics of weakly anharmonic transmons and, despite their lower computational requirements, are not sufficient for detailed characterisation. On the other hand, pulse-level simulation describes the physical system in more detail, but is then computationally heavier. Also, it is key to accurately define the physical model with experimentally confirmed parameters. When properly configured, a pulse-level simulator can be a useful asset in the development of quantum computers.

The composite sequences in general will be more effective with larger coherent errors, and greater advantages will be found in quantum systems, where control calibration is more difficult. The amplitude errors targeted here do not make up the whole picture of coherent errors, as for example inaccuracies in drive frequency and phase exist as well. These errors are not discussed in the framework of this work, but are important nonetheless. Composite sequence approaches to mitigating frequency errors have been proposed [14, 50] and form a possible future topic to explore. Furthermore, extensions to two-qubit gates have been studied [60, 61]. While the role of these methods in the pursuit of quantum advantage remains unclear, they at least offer one possibility for error mitigation.

References

[1] M. Nielsen and I. Chuang. *Quantum Computation and Quantum Information.* 10th Anniversary. Cambridge University Press, 2010.

[2] R. P. Feynman. "Simulating physics with computers". *International Journal of Theoretical Physics* 21 (1982), pp. 467–488. DOI: `10.1007/BF02650179`.

[3] P. Shor. "Algorithms for quantum computation: discrete logarithms and factoring". *Proceedings 35th Annual Symposium on Foundations of Computer Science* (1994), pp. 124–134. DOI: `10.1109/SFCS.1994.365700`.

[4] S. Woerner and D. J. Egger. "Quantum risk analysis". *npj Quantum Information* 5, 15 (2019). DOI: `10.1038/s41534-019-0130-6`.

[5] N. Stamatopoulos et al. "Option Pricing using Quantum Computers". *Quantum* 4 (2020), p. 291. DOI: `10.22331/q-2020-07-06-291`.

[6] A. Peruzzo et al. "A variational eigenvalue solver on a photonic quantum processor". *Nature Communications* 5, 4213 (2014). DOI: `10.1038/ncomms5213`.

[7] M. G. Algaba et al. "Co-Design quantum simulation of nanoscale NMR". *Physical Review Research* 4, 043089 (2022). DOI: `10.1103/PhysRevResearch.4.043089`.

[8] E. Farhi, J. Goldstone, and S. Gutmann. "A Quantum Approximate Optimization Algorithm" (2014). arXiv: `1411.4028v1 [quant-ph]`.

[9] J. Preskill. "Quantum Computing in the NISQ era and beyond". *Quantum* 2 (2018), p. 79. DOI: `10.22331/q-2018-08-06-79`.

[10] M. Kjaergaard et al. "Superconducting Qubits: Current State of Play". *Annual Review of Condensed Matter Physics* 11 (2020), pp. 369–395. DOI: `10.1146/annurev-conmatphys-031119-050605`.

[11] J.-S. Li and N. Khaneja. "Control of inhomogeneous quantum ensembles". *Physical Review A* 73, 030302 (2006). DOI: `10.1103/PhysRevA.73.030302`.

[12] E. Collin et al. “NMR-like Control of a Quantum Bit Superconducting Circuit”. *Physical Review Letters* 93, 157005 (2004). DOI: `10.1103/PhysRevLett.93.157005`.

[13] B. T. Torosov and N. V. Vitanov. “Experimental Demonstration of Composite Pulses on IBM’s Quantum Computer”. *Physical Review Applied* 18, 034062 (2022). DOI: `10.1103/PhysRevApplied.18.034062`.

[14] H. K. Cummins, G. Llewellyn, and J. A. Jones. “Tackling systematic errors in quantum logic gates with composite rotations”. *Physical Review A* 67, 042308 (2003). DOI: `10.1103/PhysRevA.67.042308`.

[15] S. Wimperis. “Broadband, Narrowband, and Passband Composite Pulses for Use in Advanced NMR Experiments”. *Journal of Magnetic Resonance, Series A* 109 (1994), pp. 221–231. DOI: `10.1006/jmra.1994.1159`.

[16] M. M. Ibrahim et al. “Evaluation of Parameterized Quantum Circuits with Cross-Resonance Pulse-Driven Entanglers”. *IEEE Transactions on Quantum Engineering* (2022). DOI: `10.1109/TQE.2022.3231124`.

[17] T. Alexander et al. “Qiskit pulse: programming quantum computers through the cloud with pulses”. *Quantum Science and Technology* 5, 044006 (2020). DOI: `10.1088/2058-9565/aba404`.

[18] F. Marxer et al. “Long-Distance Transmon Coupler with cz-Gate Fidelity above 99.8 %”. *PRX Quantum* 4, 010314 (2023). DOI: `10.1103/PRXQuantum.4.010314`.

[19] M. Nakahara and T. Ohmi. *Quantum Computing.* CRC Press, 2008.

[20] N. D. Mermin. *Quantum Computer Science.* Cambridge University Press, 2007.

[21] A. Blais et al. “Circuit quantum electrodynamics”. *Reviews of Modern Physics* 93, 025005 (2021). DOI: `10.1103/RevModPhys.93.025005`.

[22] S. Rasmussen et al. “Superconducting Circuit Companion—an Introduction with Worked Examples”. *PRX Quantum* 2, 040204 (2021). DOI: `10.1103/PRXQuantum.2.040204`.

[23] D. C. McKay et al. “Efficient Z gates for quantum computing”. *Physical Review A* 96, 022330 (2017). DOI: `10.1103/PhysRevA.96.022330`.

[24] D. E. Deutsch. “Quantum computational networks”. *Proceedings of the Royal Society of London. A. Mathematical and Physical Sciences* 425 (1989), pp. 73–90. DOI: `10.1098/rspa.1989.0099`.

[25] D. van Delft and P. Kes. “The discovery of superconductivity”. *Physics Today* 63, 9 (2010), pp. 38–43. DOI: `10.1063/1.3490499`.

[26] J. Bardeen, L. N. Cooper, and J. R. Schrieffer. “Theory of Superconductivity”. *Physical Review* 108 (1957), pp. 1175–1204. DOI: `10.1103/PhysRev.108.1175`.

[27] T. T. Heikkilä. *The physics of nanoelectronics transport and fluctuation phenomena at low temperatures.* 1st ed. Oxford University Press, 2013.

[28] P. Krantz et al. “A Quantum Engineer’s Guide to Superconducting Qubits” (2019). DOI: `10.1063/1.5089550`.

[29] Y. Nakamura, Y. A. Pashkin, and J. S. Tsai. “Coherent control of macroscopic quantum states in a single-Cooper-pair box”. *Nature* 398 (1999), pp. 786–788. DOI: `10.1038/19718`.

[30] J. Koch et al. “Charge-insensitive qubit design derived from the Cooper pair box”. *Physical Review A* 76, 042319 (2007). DOI: `10.1103/PhysRevA.76.042319`.

[31] J. M. Kreikebaum et al. “Improving wafer-scale Josephson junction resistance variation in superconducting quantum coherent circuits”. *Superconductor Science and Technology* 33, 06LT02 (2020). DOI: `10.1088/1361-6668/ab8617`.

[32] F. Motzoi et al. “Simple Pulses for Elimination of Leakage in Weakly Nonlinear Qubits”. *Physical Review Letters* 103, 110501 (2009). DOI: `10.1103/PhysRevLett.103.110501`.

[33] J. M. Gambetta et al. “Analytic control methods for high-fidelity unitary operations in a weakly nonlinear oscillator”. *Physical Review A* 83, 012308 (2011). DOI: `10.1103/PhysRevA.83.012308`.

[34] D. P. DiVincenzo. “The Physical Implementation of Quantum Computation”. *Fortschritte der Physik* 48 (2000), pp. 771–783. DOI: `10.1002/1521-3978(200009)48:9/11<771::AID-PROP771>3.0.CO;2-E`.

[35] J. Tuorila et al. “Efficient protocol for qubit initialization with a tunable environment”. *npj Quantum Information* 3, 27 (2017). DOI: `10.1038/s41534-017-0027-1`.

[36] J. J. Wallman and J. Emerson. “Noise tailoring for scalable quantum computation via randomized compiling”. *Physical Review A* 94, 052325 (2016). DOI: `10.1103/PhysRevA.94.052325`.

[37] A. Greene et al. “Error mitigation via stabilizer measurement emulation” (2021). arXiv: `2102.05767v1 [quant-ph]`.

[38] F. Bloch. “Generalized Theory of Relaxation”. *Physical Review* 105 (1957), pp. 1206–1222. DOI: `10.1103/PhysRev.105.1206`.

[39] A. G. Redfield. “On the Theory of Relaxation Processes”. *IBM Journal of Research and Development* 1 (1957), pp. 19–31. DOI: `10.1147/rd.11.0019`.

[40] J. Bylander et al. “Noise spectroscopy through dynamical decoupling with a superconducting flux qubit”. *Nature Physics* 7 (2011), pp. 565–570. DOI: `10.1038/nphys1994`.

[41] R. Jozsa. “Fidelity for Mixed Quantum States”. *Journal of Modern Optics* 41 (1994), pp. 2315–2323. DOI: `10.1080/09500349414552171`.

[42] J. M. Chow et al. “Universal Quantum Gate Set Approaching Fault-Tolerant Thresholds with Superconducting Qubits”. *Physical Review Letters* 109, 060501 (2012). DOI: `10.1103/PhysRevLett.109.060501`.

[43] A. Gilchrist, N. K. Langford, and M. A. Nielsen. “Distance measures to compare real and ideal quantum processes”. *Physical Review A* 71, 062310 (2005). DOI: `10.1103/PhysRevA.71.062310`.

[44] M. Horodecki, P. Horodecki, and R. Horodecki. “General teleportation channel, singlet fraction, and quasidistillation”. *Physical Review A* 60 (1999), pp. 1888–1898. DOI: `10.1103/PhysRevA.60.1888`.

[45] B. Li et al. “Pulse-level noisy quantum circuits with QuTiP”. *Quantum* 6, 630 (2022). DOI: `10.22331/q-2022-01-24-630`.

[46] M. H. Levitt. “Composite pulses”. *Progress in Nuclear Magnetic Resonance Spectroscopy* 18 (1986), pp. 61–122. DOI: `10.1016/0079-6565(86)80005-X`.

[47] J. T. Merrill and K. R. Brown. “Progress in Compensating Pulse Sequences for Quantum Computation”. In: *Advances in Chemical Physics, Quantum Information and Computation for Chemistry*. Ed. by S. Kais. 2014, pp. 241–294.

[48] L. Xiao and J. A. Jones. "Robust logic gates and realistic quantum computation". *Physical Review A* 73, 032334 (2006). DOI: `10.1103/PhysRevA.73.032334`.

[49] R Tycko et al. "Composite pulses without phase distortion". *Journal of Magnetic Resonance* 61 (1985), pp. 90–101. DOI: `10.1016/0022-2364(85)90270-7`.

[50] K. R. Brown, A. W. Harrow, and I. L. Chuang. "Arbitrarily accurate composite pulse sequences". *Physical Review A* 70, 052318 (2004). DOI: `10.1103/PhysRevA.70.052318`.

[51] B. T. Torosov and N. V. Vitanov. "Smooth composite pulses for high-fidelity quantum information processing". *Physical Review A* 83, 053420 (2011). DOI: `10.1103/PhysRevA.83.053420`.

[52] Atos Quantum Learning Machine. 2022. URL: `https://atos.net/en/solutions/quantum-learning-machine` (visited on 12/08/2022).

[53] CSC Kvasi Service Description. 2022. URL: `https://research.csc.fi/-/kvasi` (visited on 12/08/2022).

[54] J. R. Johansson, P. D. Nation, and F. Nori. "QuTiP 2: A Python framework for the dynamics of open quantum systems" (2012). DOI: `10.1016/j.cpc.2012.11.019`.

[55] P. Jurcevic et al. "Demonstration of quantum volume 64 on a superconducting quantum computing system". *Quantum Science and Technology* 6, 025020 (2021). DOI: `10.1088/2058-9565/abe519`.

[56] F. Arute et al. "Quantum supremacy using a programmable superconducting processor". *Nature* 574 (2019), pp. 505–510. DOI: `10.1038/s41586-019-1666-5`.

[57] S. Lazăr et al. "Calibration of Drive Non-Linearity for Arbitrary-Angle Single-Qubit Gates Using Error Amplification" (2022). arXiv: `2212.01077 [quant-ph]`.

[58] *Qiskit Experiments 0.4 Documentation.* URL: `https://qiskit.org/documentation/experiments/` (visited on 08/02/2023).

[59] R. Blume-Kohout et al. "Robust, self-consistent, closed-form tomography of quantum logic gates on a trapped ion qubit" (2013). arXiv: `1310.4492v1 [quant-ph]`.

[60] S. S. Ivanov and N. V. Vitanov. “Composite two-qubit gates”. *Physical Review A* 92, 022333 (2015). DOI: `10.1103/PhysRevA.92.022333`.

[61] Y Tomita, J. T. Merrill, and K. R. Brown. “Multi-qubit compensation sequences”. *New Journal of Physics* 12, 015002 (2010). DOI: `10.1088/1367-2630/12/1/015002`.

A The rotating frame: transformation and approximation

In the laboratory frame, the Hamiltonian operator of a quantum harmonic oscillator, $H_{\mathrm{QHO}} = \omega a^\dagger a$, causes the qubit state rotate at a frequency ω. This in turn propagates a state $|\psi_0\rangle$ as $|\psi(t)\rangle = U_{\mathrm{QHO}} |\psi_0\rangle = \exp(-iH_{\mathrm{QHO}}t) |\psi_0\rangle$. The goal of the rotating frame transformation is to go into the qubit's frame, effectively cancelling the rotation. In two-level systems, in the laboratory frame the Bloch vector rotates around the Bloch sphere at frequency ω, and in the rotating frame the spectator rotates around the sphere at the same frequency seeing effectively a stationary system. Here, the unitary transformation from laboratory to rotating frame and a following rotating wave approximation are presented in detail.

In order to cancel out the rotation with frequency ω, one needs to create a unitary transformation that cancels the time-dependent propagation of that term. Therefore, it can be identified that the transformation is

$$U_{\mathrm{rf}} = U_{\mathrm{QHO}}^\dagger = e^{iH_{\mathrm{QHO}}t} = e^{i\omega a^\dagger a t}, \tag{66}$$

and in the rotating frame the system evolves as $|\psi_{\mathrm{rf}}(t)\rangle = U_{\mathrm{rf}} |\psi_0\rangle$. The corresponding rotating frame Hamiltonian can be solve from the Schrödinger equation

$$\begin{aligned} i\partial_t |\psi_{\mathrm{rf}}(t)\rangle =& i\partial_t(U_{\mathrm{rf}}(t) |\psi\rangle) \\ =& i(\partial_t U_{\mathrm{rf}}) |\psi_0\rangle + iU_{\mathrm{rf}}(\partial_t |\psi_0\rangle) \\ =& i\dot{U}_{\mathrm{rf}}U_{\mathrm{rf}}^\dagger |\psi_{\mathrm{rf}}(t)\rangle + U_{\mathrm{rf}}H_{\mathrm{QHO}} |\psi_0\rangle \\ =& \underbrace{\left[i\dot{U}_{\mathrm{rf}}U_{\mathrm{rf}}^\dagger + U_{\mathrm{rf}}H_{\mathrm{QHO}}U_{\mathrm{rf}}^\dagger\right]}_{=\tilde{H}_{\mathrm{QHO}}} |\psi_{\mathrm{rf}}(t)\rangle, \end{aligned} \tag{67}$$

where $\tilde{H}_{\mathrm{QHO}}$ represents H_{QHO} in the new frame [28]. It will be shown below that $\tilde{H}_{\mathrm{QHO}}$ vanishes.

Next, the same transformation is studied for the driven Duffing Hamiltonian (Eq. 43) representing the weakly anharmonic and capacitively controlled qubit. As implied in Eq. (67) a Hamiltonian changes under a unitary transformation U as $H \to UHU^\dagger + i\dot{U}U^\dagger$. In the following the Baker-Campbell-Haussdorf formula

$$e^{A}Be^{-A} = B + [A,B] + \frac{1}{2}[A,[A,B]] + \ldots \frac{1}{n!}[\overbrace{A,[A,\ldots[A}^{nA\text{'s}},B]\ldots] = \sum_{n=0}^{\infty}\frac{[(A)^n,B]}{n!}, \tag{68}$$

where $[(A)^n, B]$ is the iterative commutator, is heavily used. Additionally, the creation and annihilation operators satisfy the commutation relation $[a, a^\dagger] = 1$, equivalent to

$$aa^\dagger - a^\dagger a = 1 \quad \Leftrightarrow \quad aa^\dagger = a^\dagger a + 1 \quad \Leftrightarrow \quad a^\dagger a = aa^\dagger - 1. \tag{69}$$

The first term of the transformation is

$$\begin{aligned} U_{\text{rf}}HU_{\text{rf}}^\dagger &= e^{i\omega a^\dagger at}\left[\omega a^\dagger a + \frac{\alpha}{2}a^\dagger a^\dagger aa - i\Omega(t)(a - a^\dagger)\right]e^{-i\omega a^\dagger at} \qquad (70)\\ &= \omega e^{i\omega a^\dagger at}\left[a^\dagger a\right]e^{-i\omega a^\dagger at} + \frac{\alpha}{2}e^{i\omega a^\dagger at}\left[a^\dagger a^\dagger aa\right]e^{-i\omega a^\dagger at}\\ &\quad - i\Omega(t)e^{i\omega a^\dagger at}\left[(a - a^\dagger)\right]e^{-i\omega a^\dagger at}. \qquad (71) \end{aligned}$$

The terms above transform as:
1)

$$\begin{aligned} \omega e^{i\omega a^\dagger at}\left[a^\dagger a\right]e^{-i\omega a^\dagger at} &= \omega\Big[a^\dagger a + \underbrace{[i\omega a^\dagger at, a^\dagger a]}_{*} + \frac{1}{2}[i\omega a^\dagger at,[i\omega a^\dagger at, a^\dagger a]] + \ldots\Big]\\ &\qquad\qquad * = i\omega t a^\dagger aa^\dagger a - i\omega t a^\dagger aa^\dagger a = 0\\ &= \omega a^\dagger a \end{aligned} \tag{72}$$

2)

$$\begin{aligned} &\frac{\alpha}{2}e^{i\omega a^\dagger at}\left[a^\dagger a^\dagger aa\right]e^{-i\omega a^\dagger at}\\ &= \frac{\alpha}{2}e^{i\omega a^\dagger at}\left[a^\dagger(aa^\dagger - 1)a\right]e^{-i\omega a^\dagger at} = \frac{\alpha}{2}\left[e^{i\omega a^\dagger at}\left[a^\dagger aa^\dagger a\right]e^{-i\omega a^\dagger at} - a^\dagger a\right]\\ &= \frac{\alpha}{2}\Big[a^\dagger aa^\dagger a + \underbrace{[i\omega a^\dagger at, a^\dagger aa^\dagger a]}_{*} + \frac{1}{2}[i\omega a^\dagger at,[i\omega a^\dagger at, a^\dagger aa^\dagger a]] + \ldots - a^\dagger a\Big]\\ &\qquad * = i\omega t a^\dagger aa^\dagger aa^\dagger a - i\omega t a^\dagger aa^\dagger aa^\dagger a = 0\\ &= \frac{\alpha}{2}\left[a^\dagger aa^\dagger a - a^\dagger a\right] = \frac{\alpha}{2}a^\dagger a^\dagger aa \end{aligned} \tag{73}$$

3) The control term can be investigated through the transformations of the ladder operators. For the annihilation operator:

$$\begin{aligned} e^{i\omega a^\dagger a t} a e^{-i\omega a^\dagger a t} &= a + \underbrace{[i\omega a^\dagger a t, a]}_{*} + \frac{1}{2} \underbrace{[i\omega a^\dagger a t, [i\omega a^\dagger a t, a]]}_{**} + \ldots \\ * &= i\omega t a^\dagger a a - i\omega t a a^\dagger a = i\omega t a^\dagger a a - i\omega t a^\dagger a a - i\omega t a = -i\omega t a \\ ** &= \omega^2 t^2 a^\dagger a a - \omega^2 t^2 a a^\dagger a = \omega^2 t^2 a^\dagger a a - \omega^2 t^2 a^\dagger a a - \omega^2 t^2 a = -\omega^2 t^2 a \\ &= a\left(1 - i\omega t - \frac{1}{2}\omega^2 t^2 - \ldots\right) = e^{-i\omega t} a. \end{aligned} \tag{74}$$

With similar arguments $a^\dagger$ is transformed to $e^{i\omega t} a^\dagger$. Therefore the complete control term is

$$\begin{aligned} -i\Omega(t) e^{i\omega a^\dagger a t} \left[(a - a^\dagger)\right] e^{-i\omega a^\dagger a t} &= -i\Omega(t)\left(e^{-i\omega t} a - e^{i\omega t} a^\dagger\right) \\ &= -i\Omega(t)\left((\cos\omega t - i\sin\omega t)a - (\cos\omega t + i\sin\omega t)a^\dagger\right) \\ &= \Omega(t)\left[\cos\omega t(-i(a - a^\dagger)) - \sin\omega t(a + a^\dagger)\right]. \end{aligned} \tag{75}$$

The second term in the unitary transformation of the Hamiltonian is

$$i\dot{U}_{\mathrm{rf}} U_{\mathrm{rf}}^\dagger = i\left(i\omega a^\dagger a\right) e^{i\omega a^\dagger a t} e^{-i\omega a^\dagger a t} = -\omega a^\dagger a. \tag{76}$$

This cancels the QHO term of the original Hamiltonian as promised earlier, and thus the Hamiltonian in the rotating frame has the form

$$H_{\mathrm{rf}} = \frac{\alpha}{2} a^\dagger a^\dagger a a + \Omega(t)\left[\cos\omega t(-i(a - a^\dagger)) - \sin\omega t(a + a^\dagger)\right]. \tag{77}$$

The form of the time-dependent drive $\Omega(t)$ will be discussed next. Omitting possible constant factors, it can often be considered a sinusoidal signal multiplied by an envelope function, i.e

$$\Omega(t) = s(t)\sin(\omega t + \phi) = s(t)(\underbrace{\cos\phi}_{=I}\sin\omega t + \underbrace{\sin\phi}_{=Q}\cos wt), \tag{78}$$

the I and Q are the in-phase and out-of-phase signals, respectively. The driving frequency is assumed to be identical to the qubit frequency, in other words the qubit is driven on-resonance. The second term in Eq. (77) is then

$$\begin{aligned}
&s(t)\,(I\sin\omega t + Q\cos\omega t)\left(\cos\omega t(-i(a-a^\dagger)) - \sin\omega t(a+a^\dagger)\right)\\
=\;& s(t)\left((I\sin\omega t\cos\omega t + Q\cos^2\omega t)(-i(a-a^\dagger))\right.\\
&\left. -\,(I\sin^2\omega t + Q\cos\omega t\sin\omega t)(a+a^\dagger)\right.\\
=\;& \frac{s(t)}{2}\left((I\sin 2\omega t + Q(\cos 2\omega t - 1))(-i(a-a^\dagger))\right.\\
&\left. -\,(I(1-\cos 2\omega t) + Q\sin 2\omega t)(a+a^\dagger)\right. . \qquad (79)
\end{aligned}$$

By applying the rotating wave approximation, the high-frequency (2ω) terms can be neglected with the reasoning that the fast oscillations average to zero. Finally, the rotating frame Hamiltonian after the rotating wave approximation is

$$H_{\mathrm{rf}} = \frac{\alpha}{2}a^\dagger a^\dagger a a - \frac{s(t)}{2}\left(I(a+a^\dagger) + Q(-i(a-a^\dagger))\right). \qquad (80)$$